

# A Self-Organizing Maps Analysis of Wintertime North Pacific Jet Stream Variability

MARIA M. MADSEN<sup>a</sup> AND JONATHAN E. MARTIN<sup>a</sup>

<sup>a</sup> *Department of Atmospheric and Oceanic Sciences, University of Wisconsin–Madison, Madison, Wisconsin*

(Manuscript received 14 July 2022, in final form 31 October 2022)

**ABSTRACT:** Previous research regarding the intraseasonal variability of the wintertime Pacific jet has employed empirical orthogonal function (EOF)/principal component (PC) analysis to characterize two leading modes of variability: a zonal extension or retraction and a  $\sim 20^\circ$  meridional shift of the jet exit region. These leading modes are intimately tied to the large-scale structure, sensible weather phenomena, and forecast skill in and around the vast North Pacific basin. However, variability within the wintertime Pacific jet and the relative importance of tropical and extratropical processes in driving such variability, is poorly understood. Here, a self-organizing maps (SOM) analysis is applied to 73 Northern Hemisphere cold seasons of 250-hPa zonal winds from the NCEP–NCAR reanalysis data to identify 12 characteristic physical jet states, some of which resemble the leading EOF Pacific jet patterns and combinations of them. Examination of teleconnection patterns such as El Niño–Southern Oscillation (ENSO) and the Madden–Julian oscillation (MJO) provide insight into the varying nature of the 12 SOM nodes at inter- and intraseasonal time scales. These relationships suggest that the hitherto more common EOF/PC analysis of jet variability obscures important subtleties of jet structure, revealed by the SOM analysis, which bear on the underlying physical processes associated with Pacific jet variability as well as the nature of its downstream impacts.

**KEYWORDS:** Teleconnections; Jets; Intraseasonal variability; Clustering; Machine learning; Neural networks

## 1. Introduction

Among the most ubiquitous and influential features of the general circulation of the atmosphere are the meandering, tropopause-level wind speed maxima known as jet streams. The Northern Hemisphere (NH) jet stream is characterized by two regions of maximum intensity—one over the North Pacific extending from the coast of Asia into the central Pacific and another from the coast of North America into the Atlantic Ocean. During the NH winter [November–March (NDJFM)] when the meridional temperature gradient strengthens, both the climatological intensity and zonal extent of the North Pacific jet (NPJ) increase, reaching their zeniths in February before weakening and retracting thereafter (Newman and Sardeshmukh 1998). Throughout the same season, the NPJ undergoes large and often rapid variations in both its zonal extent as well as the meridional deflection of its exit region. These modes of variability of the NPJ have been the focus of a number of recent studies (e.g., Athanasiadis et al. 2010; Jaffe et al. 2011; Griffin and Martin 2017; Breeden and Martin 2018, 2019; Winters et al. 2019a,b). As one of the most important features at the interface between the large-scale general circulation and the life cycle of individual weather systems, there is both theoretical and operational incentive to improve understanding of jet variability.

Current understanding of the intraseasonal variability of the wintertime NPJ is centered on the two predominant patterns mentioned above: a zonal extension or retraction of the jet exit region between  $160^\circ\text{E}$  and  $120^\circ\text{W}$  and a  $\sim 20^\circ$  meridional shift of its exit region (Athanasiadis et al. 2010; Jaffe et al. 2011; Delcambre et al. 2013). These leading patterns are associated with basin-scale anomalies in the Pacific that have

substantial impact on the synoptic-scale structure and downstream sensible weather. For example, Chu et al. (1993) showed that a zonally retracted jet was associated with a wet Hawaiian winter, whereas an extended jet was associated with an extremely dry winter. Additionally, in constructing a climatology of subtropical kona cyclones over Hawaii, Otkin and Martin (2004) found that a retracted NPJ is linked to increased frequency of such storms. Similarly, Jaffe et al. (2011) examined 19 cold season jet retractions that occurred within 28 years of NCEP–NCAR reanalysis data and found that variability within the Pacific storm track occurs in tandem with retraction events. Composite analysis of the retraction events revealed that prior to the retraction, enhanced storm track density downstream and poleward of the climatological jet exit region prevails. After the retraction events, however, the same region has suppressed storm track density, while enhanced storm track density appears in the central subtropical Pacific. Retraction events were also associated with a rapid onset of a negative Pacific–North America (PNA) pattern (Wallace and Gutzler 1981). Over the 10 days surrounding each event, both 500-hPa geopotential height and sea level pressure (SLP) anomalies switched polarity from negative to positive in the North Pacific, exhibited an equivalent barotropic structure with broad areal extent, and had magnitudes exceeding 200 m and 20 hPa, respectively.

In addition to sensible weather impacts in Hawaii and elsewhere in the Pacific basin, recent studies have demonstrated impacts over North America. Griffin and Martin (2017) showed that jet extensions and poleward shifts were both associated with enhanced 250-hPa cyclonic circulations in the central North Pacific and 850-hPa low-level warm anomalies over North America. For jet extensions, the warm anomalies were localized over western North America whereas for poleward

---

*Corresponding author:* Maria M. Madsen, m.madsen@ou.edu

DOI: 10.1175/JCLI-D-22-0452.1

© 2023 American Meteorological Society. For information regarding reuse of this content and general copyright information, consult the [AMS Copyright Policy](#) ([www.ametsoc.org/PUBSReuseLicenses](http://www.ametsoc.org/PUBSReuseLicenses)).

shifts, they were localized over north-central North America. Conversely, jet retractions and equatorward shifts led to enhanced 250-hPa anticyclonic circulations in the central North Pacific and low-level cold anomalies over western North America. These results were corroborated by [Winters et al. \(2019a\)](#) who tied extreme temperature events (ETEs) in North America to the leading NPJ patterns. Using a NPJ phase diagram constructed from the two leading empirical orthogonal functions (EOFs) of 250-hPa zonal wind, they found that warm ETEs on the U.S. West Coast are frequently characterized by an evolving jet extension and equatorward deflection in the 10 days preceding the event. Conversely, cold ETEs on the west coast and warm ETEs on the east coast occur most frequently in the days following jet retractions. This is consistent with studies showing negative PNA patterns associated with jet retraction events (e.g., [Jaffe et al. 2011](#); [Breedon and Martin 2018](#)). Additionally, equatorward shifts of the jet preceded most cold ETEs on the U.S. East Coast.

Using the same NPJ phase diagram employed in [Winters et al. \(2019a\)](#), [Winters et al. \(2019b\)](#), showed that the pattern, and changes between patterns, of the NPJ has an apparent impact on medium-range forecast skill over North America. The study analyzed 30 years of Global Ensemble Forecast System (GEFS) reforecasts to conclude that the greatest forecast skill occurred in conjunction with an extended or poleward deflected jet, whereas the worst skill occurred in conjunction with a retracted or equatorward shifted jet. Additionally, there was reduced forecast skill during a transition between extensions, retractions, and deflections poleward and equatorward.

Despite recent work demonstrating the substantial impact that NPJ variability has on the large-scale structure, sensible weather phenomena, and forecast skill in and around the vast North Pacific basin, variability within the NPJ, and its relationship to extratropical and tropical processes, is poorly understood. Better understanding of such variability promises new insight into aspects of tropical/extratropical interaction and may provide additional guidance in the medium-range forecasting of some extreme events. As such, the present paper seeks to expand the characterization of NPJ variability by viewing it through application of self-organizing maps (SOM) ([Kohonen 1982](#)) and empirical orthogonal function/principal component (EOF/PC) analyses.

The remainder of the paper is structured in the following way. [Section 2](#) provides details of the dataset and methodology, including an in-depth description of the SOM analysis. The structure of the various jet regimes revealed in the SOM analysis and their projections onto an EOF1/EOF2 phase space are analyzed in [section 3](#). [Section 4](#) analyzes teleconnections associated with the SOM-identified jet regimes. Last, [section 5](#) provides the conclusions.

## 2. Data and methodology

The use of EOF analysis to decompose and filter spatiotemporal data is a common form of exploratory data analysis that has long been a central part of weather and climate research. EOF/PC analysis identifies a hierarchy of orthogonal spatial patterns most representative of the modes of variability within

a state space (the EOFs), as well as a time series of coefficient values for each EOF that represents the magnitude of the EOF's contribution to the state space through time (the principal components, or PCs) (e.g., [Lorenz 1956](#); [Kutzbach 1967](#); [Cohen 1983](#); [Smith et al. 1996](#); [Hannachi 2004](#); [Wilks 2011](#)). The leading EOFs are the patterns explaining the largest amount of variance of the dataset. Wintertime NPJ variability has been traditionally studied with the use of EOF/PC analysis (e.g., [Athanasiadis et al. 2010](#); [Jaffe et al. 2011](#); [Griffin and Martin 2017](#); [Winters et al. 2019a,b](#)). Previous work has identified the leading mode, EOF1, as an extension/retraction, with anomalies nearly along the climatological jet exit region. The next leading mode, EOF2, is characterized by anomalies displaced poleward or equatorward of the exit region.

Although previous research on jet variability has relied heavily upon EOF analysis, the leading patterns explain only ~30% of the total variance and, by construction, each mode is linearly independent from the other. This can lead to physically unrealistic interpretations, as atmospheric patterns are typically nonorthogonal. Therefore, EOF analysis, while important to developing understanding, provides a rather limited view of NPJ variability. Consequently, this work also employs a self-organizing maps (SOM) analysis. SOM analysis is free from the orthogonality constraint of EOF/PC analysis and incorporates the nonlinear nature of jet stream variability. The inclusion of both linear and nonlinear aspects is a significant advantage of the SOM. This statistical technique has recently been applied to meteorological datasets in both synoptic climatologies (e.g., [Hewitson and Crane 2002](#); [Hope et al. 2006](#); [Lynch et al. 2006](#); [Cassano et al. 2006](#); [Reusch et al. 2007](#); [Schuenemann et al. 2009](#); [Johnson and Feldstein 2010](#)) as well as examinations of climate model output (e.g., [Skific et al. 2009a,b](#); [Schuenemann and Cassano 2009, 2010](#)). The use of SOMs in this work provides a less subjective, more physical, and versatile visualization tool for characterizing NPJ variability that complements, rather than replaces, traditional EOF/PC analysis.

### *Self-organizing maps*

SOMs is a method within the field of artificial neural networks that organizes large, multidimensional datasets into finite arrays of recurring *physical* patterns ([Kohonen 2001](#)). This method has been gaining popularity over the last few decades and applied to a wide range of atmospheric and oceanic phenomena for feature extraction and classification. For example, [Hewitson and Crane \(2002\)](#) employed SOMs to characterize temporal changes in synoptic scale circulation. [Reusch et al. \(2007\)](#) examined nonlinear aspects of North Atlantic Oscillation (NAO) variability through applying SOMs to December–February mean sea level pressure data. More recently, [Gervais et al. \(2016\)](#) used SOMs to characterize future changes in atmospheric variability, and [Gu and Gervais \(2021\)](#) applied SOMs to investigate North Atlantic and North Pacific decadal climate prediction. Unlike EOF/PC analysis and other cluster methods in which the data are assumed to be stationary, SOMs treats the data as a continuum.

The SOM in this study utilizes batch training, as it is the most computationally efficient with larger datasets (Kohonen 1998; Vesanto et al. 2000; Liu et al. 2006). Unlike sequential training, the batch training process does not specify a learning rate function; rather, the weight vector  $\mathbf{m}_i$  adjusts the reference vectors by

$$\mathbf{m}_i(t+1) = \frac{\sum_{j=1}^M n_j h_{ij}(t) \bar{x}_j}{\sum_{j=1}^M n_j h_{ij}(t)}, \quad (1)$$

where  $M$  is the user-determined number of groups into which the data are partitioned,  $t$  is each learning iteration,  $\bar{x}_j$  is the mean of the  $n$  input vectors within the current group, and  $h_{ij}$  is the neighborhood function. An Epanechnikov neighborhood (“ep”) function is selected for its higher performance in comparison to three other neighborhood functions available in the Matlab SOM toolbox (Vesanto et al. 2000; Liu et al. 2006). The “ep” function updates neighboring nodes by

$$h_{ci} = \max[0, 1 - (\sigma_t - d_{ci})^2], \quad (2)$$

in which a neighborhood radius of influence at time  $t$ ,  $\sigma_t$ , is specified, and  $d_{ci}$  is the distance between SOM nodes  $c$  and  $i$ . The SOM is run with two sets of trainings of decreasing neighborhood radius. The initial batch training uses a larger neighborhood radius of influence equal to the size of the smaller SOM grid dimension (3, in the present study). The training iterates for 10 times the length of the input vector and creates a broad pattern distribution. A second training ( $\sigma_t = 1$ ) fine-tunes the SOM nodes based on the distribution from the resultant initial batch training. The SOM iterates through this process until a mean quantization error is minimized for the entire collection of nodes. The result is a large SOM array comprised of the updated reference vectors which is then converted into a two-dimensional matrix of maps. The resulting matrix of nodes consists of the most representative physical patterns spanning the continuum of, in this analysis, the zonal 250-hPa winds.

The tunable parameters in the SOM, including grid size, number of iterations, neighborhood radius, and initialization, are selected to achieve a balance of low average quantization error (QE) and topographic error (TE) as well as an evenly distributed Sammon map. The QE quantifies the difference between the node average and the input vectors. Lower QE values indicate a better representation of the best matching unit (BMU) to the data. Every SOM node consists of a collection of input vectors with varying QEs as well as a mean QE. Another important map quality measure is TE, which measures the percentage of input vectors that do not have a neighboring second BMU. In a SOM map, the nodes closest to one another are most similar. Therefore, the smaller the TE, the better the SOM map quality. Last, a Sammon map illustrates the Euclidian distances between each node in the SOM grid on a two-dimensional distortion plane (Sammon 1969). A quality SOM map will have a balance of low QE and TE, and a flat, evenly distributed Sammon map.

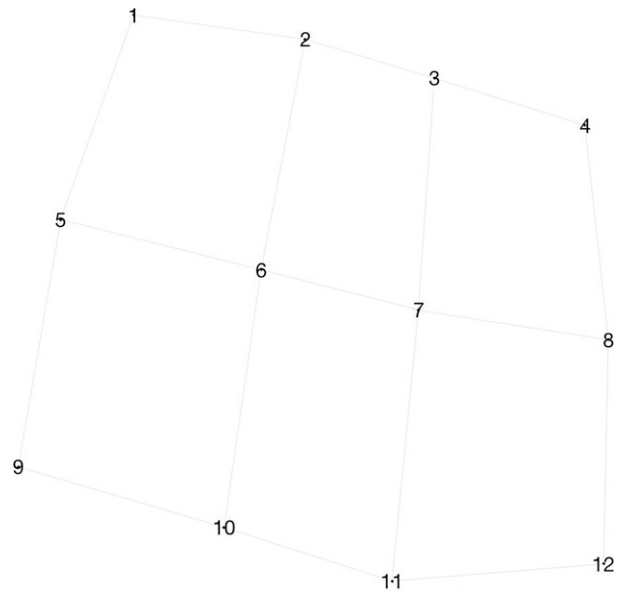


FIG. 1. Sammon map of the Euclidian distances between each node in the  $3 \times 4$  SOM grid on a two-dimensional distortion plane.

The present work employs a  $3 \times 4$  SOM grid consisting of 12 nodes. Smaller grid sizes lead to a blending of relevant patterns whereas larger grid sizes yield patterns not easily distinguishable from one another. Therefore, a  $3 \times 4$  grid size includes enough interpretable patterns to examine NPJ variability while maintaining low QE and TE errors and a well distributed Sammon map (Fig. 1). Both the EOF and SOM analyses utilize daily 250-hPa zonal wind data from the NCEP/NCAR Reanalysis (Kalnay et al. 1996), available at a  $2.5^\circ \times 2.5^\circ$  horizontal resolution. The zonal wind dataset consists of 73 cold seasons (1948/49–2020/21) in which a cold season is defined as 1 November–31 March (NDJFM). The spatial domain is  $100^\circ\text{E}$ – $120^\circ\text{W}$  and  $10^\circ$ – $80^\circ\text{N}$ , which covers nearly all of the North Pacific basin. Prior to the analyses, the long-term mean and seasonal cycle are removed from the zonal wind anomalies by subtracting a 21-day running mean of the seasonal cycle from the instantaneous 250-hPa zonal wind.

### 3. North Pacific jet regimes

#### a. Leading modes of variability

The leading modes of wintertime NPJ variability are consistent with previous findings (e.g., Athanasiadis et al. 2010; Jaffe et al. 2011; Griffin and Martin 2017; Winters et al. 2019a,b), with EOF1 (describing 14% of the variance) characterized by anomalies nearly along the climatological cold season jet exit region (Fig. 2, top), representing a jet extension in the positive EOF phase (hereafter EOF1+) or jet retraction in the negative phase (hereafter EOF1–). EOF2 (describing 10% of the variance) is characterized by anomalies displaced poleward or equatorward of the exit region (Fig. 2, bottom), representing a poleward deflection in the positive phase (EOF2+) or an

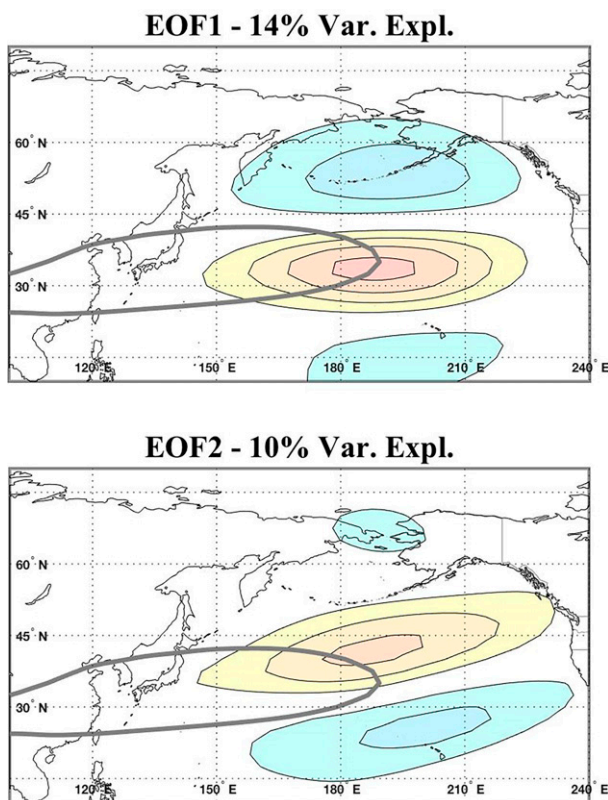


FIG. 2. EOF pattern of the 250-hPa zonal wind over the North Pacific. Perturbations are shaded ( $\text{m s}^{-1}$ ) every  $4 \text{ m s}^{-1}$  starting at 4 ( $-4$ ). Mean  $40 \text{ m s}^{-1}$  isotach over the 73 cold seasons is contoured in gray. (top) EOF1 and (bottom) EOF2.

equatorward deflection in the negative phase (EOF2 $-$ ). The leading modes are also statistically well separated, as determined by applying the North et al. (1982) test.

### b. North Pacific jet SOM nodes

In conducting a SOM analysis of the 250-hPa zonal wind, 12 intraseasonal jet anomaly regimes are depicted in the SOM nodes with a frequency of occurrence (FOC) calculated by the number of cold season days falling within the associated node divided by the total number of cold season days (11 023) (Fig. 3). Additionally, the calendric listing of days characterizing each node is used to construct composites of the associated circulation patterns and downstream impacts, consisting of 500-hPa geopotential height anomalies (Z500) (Fig. 4), sea level pressure (SLP) anomalies, and 850-hPa temperature (850T) anomalies (Fig. 5).

Beginning with the upper left of the SOM grid, node 1 depicts a retraction reaching  $-20 \text{ m s}^{-1}$  located slightly south of the climatological jet exit region with a positive zonal wind anomaly between 4 and  $20 \text{ m s}^{-1}$  south of the Aleutian Islands (Fig. 3a). The zonal wind anomalies are attended by a positive Z500 anomaly over the North Pacific and a weaker sprawling cyclonic anomaly between northeast Russia and western Canada (Fig. 4a). At the surface, a weak positive SLP

anomaly is centered near  $160^\circ\text{W}$ , with an even weaker negative SLP anomaly over Alaska and Yukon (Fig. 5a). A small and positive 850T temperature anomaly near the date line is associated with node 1, and the FOC is 7.6%.

Another retraction is evident in node 5, with strong negative anomalies of  $-24 \text{ m s}^{-1}$  in the climatological jet exit region and weaker positive anomalies centered at  $50^\circ$  and  $15^\circ\text{N}$  (Fig. 3e). This node most closely resembles EOF1+. The tripole anomaly structure indicates a split-jet feature with mid-latitude and subtropical counterparts. The FOC for this pattern is 9%, which is the largest of the other SOM nodes depicting jet retractions. The circulation pattern associated with the strong retraction is characterized by a dominant Z500 anticyclonic anomaly centered over the North Pacific basin with a weaker cyclonic anomaly stretching from northeast Russia to western Canada (Fig. 4e). At the surface, an associated positive SLP anomaly sits over the central North Pacific, with a small tongue of weak warm 850T anomalies stretching from the center of the SLP anomaly to  $\sim 150^\circ\text{E}$  (Fig. 5e).

A stronger retraction is illustrated by node 9, with negative zonal wind anomalies between  $-4$  and  $-24 \text{ m s}^{-1}$  extending farther northeast into British Columbia than in nodes 1 and 5 and with a slightly lower FOC of 6.6%. A strip of positive zonal wind anomalies poleward of the climatological jet stretches northeast from East Asia to Alaska, while another strip of positive zonal wind anomalies equatorward of the climatological jet extends from  $150^\circ\text{E}$  into the California coast (Fig. 3i). As in node 5, the tripole anomaly structure implies a split-jet feature; however, the equatorward counterpart extends much farther east than in node 5. Circulation composites reveal a southwest-northeast-tilted positive Z500 and SLP anomaly south of the Aleutian Islands (Figs. 4i, 5i). A weaker cyclonic anomaly sits downstream off the U.S. West Coast, disconnected from a smaller cyclonic anomaly south of the anticyclone (Fig. 4i). A third weak cyclonic anomaly is evident over northeastern Russia. Localized areas of cool 850T anomalies are evident over western Canada and off of the Pacific Northwest coast, whereas a larger tongue of warm 850T anomalies stretches from the coast of Japan to south of the Aleutian Islands (Fig. 5i).

Node 8 resembles the positive phase of EOF1, with strong positive zonal wind anomalies from the climatological jet exit region to  $135^\circ\text{W}$ , weaker negative zonal wind anomalies poleward of the climatological jet, and a small area of weaker negative anomalies near  $15^\circ\text{N}$  (Fig. 3h). The FOC of this jet extension is 9.3%, which is similar to the jet retraction depicted by node 5. Associated with the jet extension is a strong surface (Fig. 5h) and Z500 cyclonic anomaly on the cyclonic shear side of the jet, a weaker positive Z500 anomaly over northwestern North America, and another weak Z500 cyclonic anomaly over eastern North America (Fig. 4h). The Z500 circulation pattern resembles a positive PNA teleconnection pattern, with the warm 850T temperature anomalies over Alaska and northeastern Canada consistent with positive PNA low-level temperature anomalies (Fig. 5h).

On the other hand, node 4 illustrates an extension located farther poleward and stretching farther eastward, with strong positive zonal wind anomalies  $5^\circ$ – $10^\circ$  poleward than those characterizing node 8 (Fig. 3d). Similarly, negative zonal wind

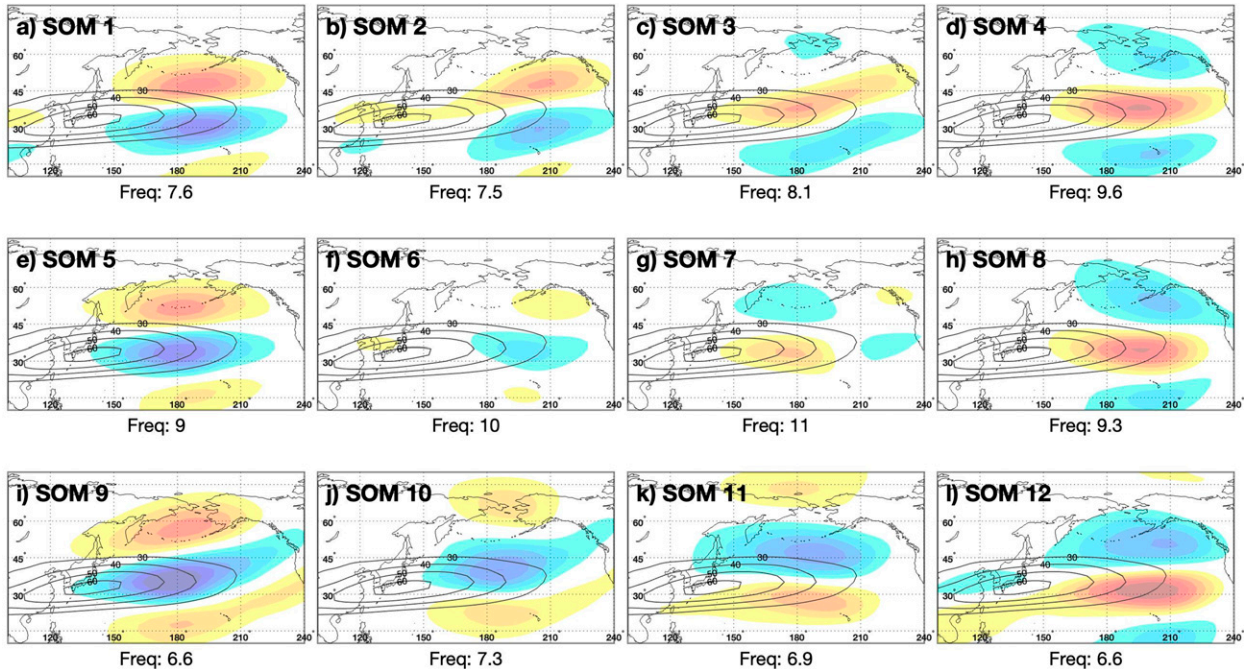


FIG. 3. SOM grid of 12 most recurring patterns of the wintertime Pacific basin 250-hPa zonal wind. Anomalies of the 250-hPa isotachs ( $\text{m s}^{-1}$ ) are shaded in warm (cool) colors every  $4 \text{ m s}^{-1}$  starting at  $4 (-4)$ . The mean 73 cold season isotachs are contoured in gray from  $30$  to  $60 \text{ m s}^{-1}$ . Below each node is the associated frequency of occurrence (%) relative to all other nodes.

anomalies lay poleward and equatorward of the climatological jet (Fig. 3d). Associated with the extension is a cyclonic Z500 and negative SLP anomaly centered south of Alaska (Figs. 4d, 5d). Two weaker areas of positive Z500 anomalies are located south and east of the cyclonic anomaly (Fig. 4d). Near the surface, warmer than normal 850T temperatures

are evident over central Canada (Fig. 5d). The FOC of node 4 is the third largest of the SOM nodes at 9.6%.

Another jet extension is evident in SOM node 12, with strong positive zonal wind anomalies in excess of  $24 \text{ m s}^{-1}$  near  $30^\circ\text{N}$ , flanked on the poleward side by an expansive negative zonal wind anomaly (Fig. 3l). This extended pattern has

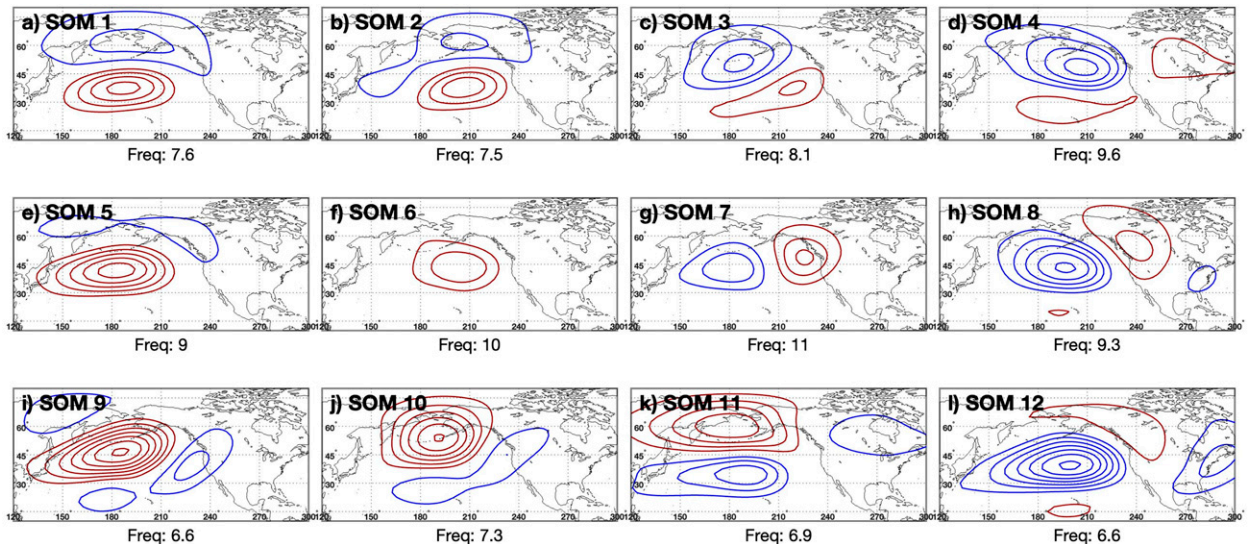


FIG. 4. Composite 500-hPa geopotential height anomalies of days within each SOM node. Below each node is the associated frequency of occurrence (%) relative to all other nodes. Positive (negative) 500-hPa geopotential height (m) anomalies are contoured in red (blue) every  $25 \text{ m}$  starting at  $25 (-25) \text{ m}$ .

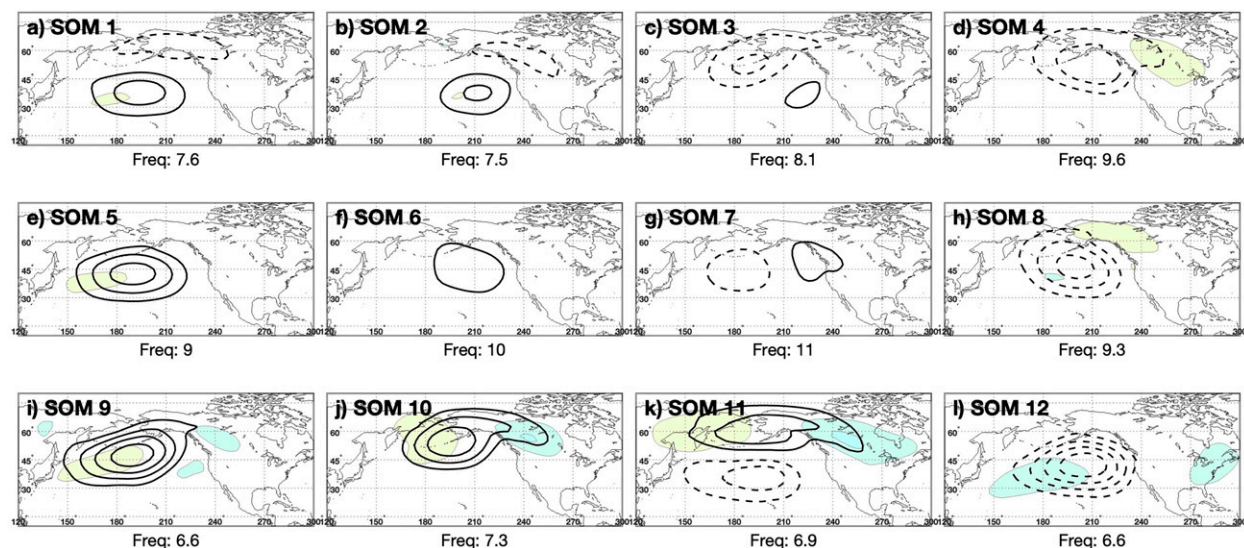


FIG. 5. As in Fig. 4, but composite positive (negative) SLP anomalies (hPa) in solid (dashed) black lines contoured every 3 hPa starting at 3 (–3) hPa and 850-hPa temperature anomalies (K) in yellow (blue) contoured every 2 K starting at 2 (–2) K.

the lowest FOC compared to the other extended nodes (4 and 8), with an FOC of 6.6%. The circulation pattern associated with node 12 resembles that of node 8, but with stronger cyclonic anomalies over the North Pacific and eastern North America displaced  $5^\circ$  equatorward and  $5^\circ$  poleward, respectively (Figs. 4i, 5l). Near the surface, 850T anomalies differ more substantially than those characterized by node 8, with cold anomalies over northeast North America and on the western flank of the cyclonic SLP anomaly (Fig. 5l).

Along the top edge of the SOM grid are variations of poleward deflections, with node 2 having the lowest FOC of 7.5% (Fig. 3b). In this node, a weak  $4 \text{ m s}^{-1}$  positive zonal wind anomaly stretches along the poleward edge of the climatological jet stream, whereas a stronger area of positive zonal wind anomalies extends northeastward into British Columbia from the climatological left jet exit region (Fig. 3b). Negative zonal wind anomalies of similar magnitude lie south of the positive anomalies. The midlevel circulation associated with node 2 depicts a weak Z500 anomaly couplet over the North Pacific, with a weaker cyclonic anomaly on the cyclonic shear side of the jet and a stronger anticyclonic anomaly on the anticyclonic shear side (Fig. 4b). At the surface, a weaker positive SLP anomaly is evident below the upper-level anticyclone, whereas a weaker negative SLP anomaly is located downstream of the upper-level cyclone (Fig. 5b).

The poleward deflection depicted by node 3, on the other hand, is characterized by a maximum positive zonal wind anomaly in the climatological left jet exit region that extends northeast and most closely resembles the positive phase of EOF2 (Fig. 3c). Weaker negative zonal wind anomalies are located over the Bering Sea and the subtropical eastern Pacific. The FOC is 8.1%, which is slightly larger than the FOC of node 2. The associated circulation pattern is characterized by a stronger Z500 cyclonic anomaly centered over the Aleutian Islands and a weaker Z500 anticyclonic

anomaly on its southeastern flank (Fig. 4c). Both Z500 anomalies over the Pacific basin have weaker associated SLP anomalies (Fig. 5c).

Equatorward deflections are evident in nodes 10 and 11, with node 10 representing 7.3% of the cold season days (Fig. 3j). In node 10, a bowed band of zonal wind anomalies between 4 and  $8 \text{ m s}^{-1}$  extends into the California coast, while a stronger area of negative zonal wind anomalies concentrates over the climatological jet exit region, extending NE into British Columbia (Fig. 3j). Another weak positive zonal wind anomaly is situated over the Bering Sea. As in nodes 5 and 9, the tripole anomaly structure implies a split-jet feature; however, the poleward midlatitude counterpart is much weaker than in the other nodes. Circulation composites reveal a positive isotropic Z500 anomaly and a SLP anomaly over the Aleutian Islands (Figs. 4j, 5j). A weaker elongated Z500 cyclonic anomaly stretches from the date line to central Canada (Fig. 4j). An area of cool 850T anomalies is evident over western Canada, whereas warm 850T anomalies sit over far northeastern Russia to the Aleutian Islands (Fig. 5j).

The zonal wind anomalies characterizing node 11 have stronger positive anomalies along the equatorward side of the climatological jet than those in node 10 and a lower FOC of 6.9% (Fig. 3k). An area of negative zonal wind anomalies sits poleward of the climatological jet, and a weaker area of positive zonal wind anomalies is evident near  $75^\circ\text{N}$ . Below the zonal wind anomalies, there is a dipole structure in the SLP and Z500 anomalies over the North Pacific, with a weaker cyclonic Z500 anomaly over Canada (Figs. 4k, 5k). Node 11 is also characterized by the largest areas of 850T anomalies, with warm anomalies over northeast Russia and cold anomalies stretching across most of Canada (Fig. 5k).

Apart from the nodes resembling variations of the leading EOF patterns, node 6 depicts the weakest anomalies, with a  $4\text{--}8 \text{ m s}^{-1}$  negative anomaly east of the climatological jet exit

TABLE 1. Characteristic residence times and quantization errors for each SOM node within the SOM grid.

SOM node	Mean residence time (days)	Max residence time (days)	Avg QE error (grid mean: 373)
Node 1	2.4	18	376
Node 2	2.3	11	362
Node 3	2.2	10	355
Node 4	2.6	15	369
Node 5	2.6	12	383
Node 6	2.2	20	370
Node 7	2.5	10	363
Node 8	2.6	11	367
Node 9	3.2	18	400
Node 10	2.6	17	387
Node 11	3.4	19	386
Node 12	4.1	43	374

region and small areas of  $4 \text{ m s}^{-1}$  positive anomalies centered over the Gulf of Alaska, south of Hawaii, and over the Sea of Japan (Fig. 3f). The mid and lower-level circulation depicts a weak anticyclonic anomaly south of Alaska and no associated 850T anomalies (Figs. 4f, 5f). Node 6 is also characterized by the second largest FOC at 10%. The highest FOC in the SOM grid is illustrated by node 7, with positive anomalies centered in the eastern half of the climatological jet indicating an enhancement of the jet exit region (Fig. 3g). Weaker and smaller  $4 \text{ m s}^{-1}$  isotachs are evident over the Aleutian Islands and off the California coast. In the midlevels, there is a negative Z500 anomaly on the cyclonic shear side of the jet and a positive Z500 anomaly downstream off the coast of British Columbia (Fig. 4g). At or near the surface, weak SLP anomalies are evident over the Pacific basin, with no cold 850T anomalies (Fig. 5g).

While there are distinct differences in zonal wind, Z500, SLP, and 850T anomalies between SOM nodes, there are also variations in average QE and node residence time (Table 1). The QE for each SOM node measures the difference between the input data vectors characterizing the node and the SOM node anomaly pattern depicted in Fig. 3. Comparing mean QE for the individual nodes can provide insight into how well each node represents the data vectors comprising it and whether stark differences between node representations exist. A smaller mean QE suggests that the pattern is better representative of the days characterizing the respective node. Comparison between the 12 QE values reveals little variation. QE values are marginally larger for nodes featuring equatorward deflections or jet retractions, with mean QE values of 400, 387, 386, and 383 for nodes 9, 10, 11, and 5, respectively. The lowest QE values are associated with poleward deflected nodes 2 and 3, with errors of 362 and 355, respectively. However, these QE departures from the mean QE of 373 are not significant and suggest that the data vectors are well-fit to the SOM nodes.

Mean residence times reflect the transient nature of the jet stream, with a range between 2.2 days (nodes 3 and 6) and 4 days (node 12). However, the maximum number of consecutive days residing within a node ranges between 10 days (nodes 3 and 7) to 43 days (node 12). The stark difference between mean and max residence times highlights the complex

nature of jet stream variability in that while short fluctuations of the jet stream are common, the jet can also exhibit a weekly to monthly persistence. The substantially larger mean residence time and persistence exhibited by node 12 suggests that it might be strongly associated with other persistent teleconnection patterns. It should also be noted that residence times are sensitive to both SOM size and configuration. To test the robustness of the longer node 12 residence time, sensitivity testing was performed on SOMs of varying sizes and configurations. This revealed that the larger residence time for a jet extension equatorward of the climatological jet stream (as in node 12) is not a methodological artifact, but rather an indication of a distinct characteristic of such extensions.

To further illustrate the relationship between the two leading EOF/PC patterns of the NPJ and the SOM patterns, days with a QE at or below the mean QE of the entire SOM grid are projected onto an EOF/PC two-dimensional phase space in Fig. 6. Following the NPJ phase space developed in Winters et al. (2019b), the leading two PCs serve as the axes of the phase space wherein the  $x$  axis is defined by PC1 (jet extension/jet retraction), and the  $y$  axis is defined by PC2 (poleward/equatorward deflection). Prior to regressing days onto the phase space, the leading PCs for each day are normalized to unit variance.

For most of the SOM nodes, there is a clear clustering in a specific quadrant of the phase space; however, some of the nodes have a larger scatter into two or more PC quadrants. Nodes 4, 8, and 12 cluster on the right half of the phase space, with node 12 clustering slightly below the positive  $x$  axis (equatorward deflected jet extension), node 8 clustering nearly along the positive  $x$  axis (jet extension), and node 4 clustering above the positive  $x$  axis (poleward deflected jet extension). Conversely, nodes 1, 5, and 9 scatter along the left half of the phase space, with node 5 clustering nearly along the negative  $x$  axis (retraction), node 1 scattered above the negative  $x$  axis (retraction and poleward deflection), and node 9 scattered below the negative  $x$  axis (retraction and equatorward deflection). The projection of days characterized by SOM node 10 averages marginally to the left of the negative  $y$  axis, denoting an equatorward deflection with a minimal retraction, whereas node 11 clusters within the bottom right of the phase space, denoting a slightly extended and equatorward deflected jet

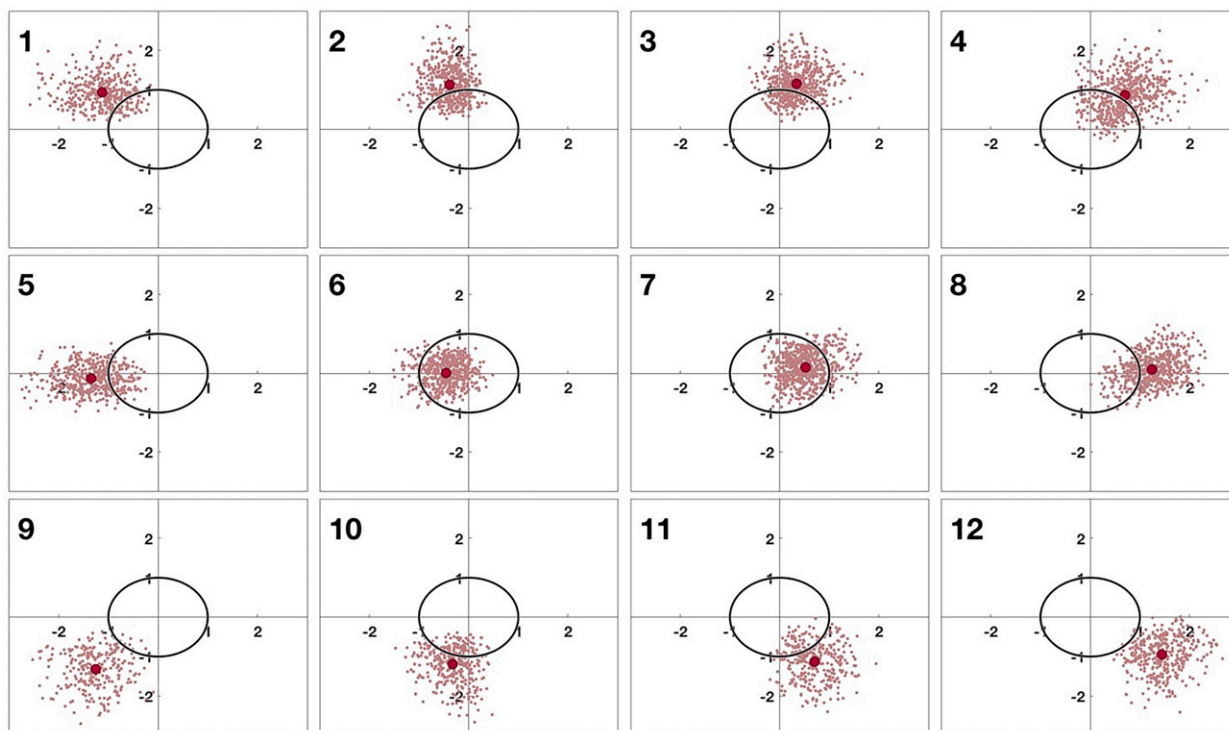


FIG. 6. State of the daily Pacific jet (maroon circles) in the 2D phase space of the leading 250-hPa zonal wind PCs for every day comprising each of the 12 SOM nodes within the 73 cold seasons (1948/49–2020/21). Black circles represent the  $1\sigma$  contour of magnitude in the EOF/PC phase space. The large red dot in each panel is the centroid of the distribution.

regime. The poleward deflections denoted by nodes 2 and 3, however, scatter along the top half of the phase space. Similarly to the equatorward deflected nodes, neither nodes 2 or 3 cluster along the positive  $y$  axis; rather, node 2 clusters to the left of the positive  $y$  axis whereas node 3 clusters to the right of the  $y$  axis. Last, nodes 6 and 7 depict the weakest anomalies and are represented as a weak jet retraction and a weak jet extension in the mean of the phase space, respectively. Overall, the two-dimensional phase space illustrates that some of the patterns comprising the 12-node SOM grid resemble the leading EOF patterns while others are clearly combinations of the leading EOFs.

### c. Variability of SOM node FOC

To gain a better understanding of the intraseasonal, interannual, and interdecadal variability of the 12 SOM nodes, cumulative frequency diagrams are generated for each of the five months within the cold season (Fig. 7), each of the 73 cold seasons (Fig. 8), and each decade beginning with 1950 (Fig. 9). For the seasonal variability, an average monthly FOC is given by first summing the total the number of days characterized by a particular node for each month and then dividing by the total number of time series days characterized by each month. A similar procedure follows for calculating FOC over 73 cold seasons, instead summing the number of days characterized by a particular SOM node for each cold season and dividing by the number of cold season days (151 days). For interdecadal FOC, the

annual FOC is averaged over seven 10-yr periods beginning with 1950–60.

The monthly distribution of the 12 SOM nodes illustrates only slight variability between months, as a 21-day smoothed seasonal cycle is removed from the data prior to the SOM analysis (Fig. 7). In November, nodes 3, 4, and 6 reach their maximum in FOC, while nodes 1, 2, and 12 occur less frequently compared to the other cold season months. The jet extension depicted by node 12, in particular, has a much lower FOC compared to other nodes (2.3%). From December into February, the FOC of node 12 increases, reaching its maximum of 10.7% in February. This is also when node 10, an equatorward deflection, reaches a minimum in FOC. Retracted nodes denoted by nodes 5 and 9 have the lowest FOC in January. By March, however, the FOC of retractions increases, with nodes 1 and 5 having a maximum in FOC of 9% and 12.1%, respectively.

Examination of FOC of the 12 SOM nodes over each cold season from 1948/49 to 2020/21 reveals substantial interannual variability, with abrupt year-to-year changes exhibited by many of the nodes (Fig. 8). Node 6 has the smallest time series variance (19.7), followed by node 3 (21.8). Regimes with larger variances are extended nodes 8 (34.2) and 12 (67.6). Along with having a considerably larger variance than the other 12 nodes, node 12 also features the largest peak in the time series—an annual cold season frequency of 42% in 1982/83. The 1982/83 cold season was also characterized by one of the strongest El Niño

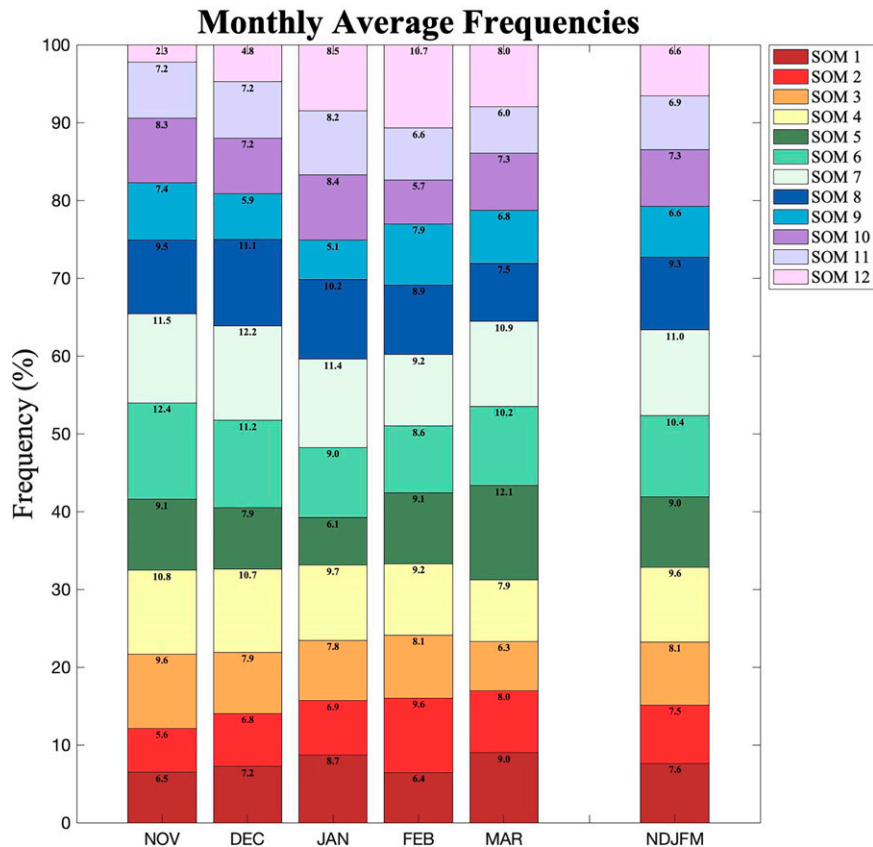


FIG. 7. Percent frequency of occurrence for each SOM node during each month of the cold season.

events on record. This is unsurprising, as prior work has shown that the increased sea surface temperatures over the central and eastern Pacific, in tandem with anomalous convection associated with an El Niño, provide a favorable environment for jet extensions (e.g., Horel and Wallace 1981; Yang et al. 2002; Li and Wettstein 2012; Cook et al. 2017). The strong El Niño cold seasons from 1957/58 to 1997/98 are also characterized by peaks in node 12 FOC, with a frequency of 19% and 30%, respectively. In fact, there is a 0.54 correlation between the time series of node 12 FOC and the time series of the seasonal mean Niño-3.4 index (ESRL), which is the highest correlation coefficient of all 12 nodes. Comparison of other extended nodes (4 and 8) to the interannual variability in node 12 reveals that there is low correlation between them. Although there are some years in which peaks in node 12 FOC are collocated with peaks in nodes 4 and/or 8, it is weakly correlated to the other time series. Similarly weak relationships are illustrated between retractions (1, 5, 9) and poleward deflections (9, 10, 11). However, the correlation between the FOC of equatorward deflected nodes 2 and 3 is 0.65, exceeding the correlation between any other pair of nodes which all fell below 0.40. Last, a linear regression performed on each of the 12 time series revealed no statistically significant trend in FOC over time.

A look at decadal variability of the SOM grid distribution also reveals the absence of a significant trend in FOC (Fig. 9).

However, some nodes exhibit stronger decadal variability than others. For example, extended node 12 increased in FOC between 1950 and 1990, beginning with an FOC of 3.9% in the 1950s and reaching a maximum FOC of 10.9% in the 1990s, before decreasing again. The decade between 1980 and 1990 was characterized by a larger frequency of jet extensions overall (nodes 4, 8, and 12). The maximum in FOC of extended nodes is attended by lower frequencies of retracted nodes 5 and 9. Most of the nodes, however, exhibit a seesawing of mild FOC fluctuations over the seven decades.

#### 4. SOM node teleconnections

As demonstrated in previous studies, large-scale atmospheric teleconnection patterns are related to fluctuations within the NPJ, and thus, are likely tied to the intraseasonal and interannual frequency distributions of the 12 SOM nodes (e.g., Wallace and Gutzler 1981; Horel and Wallace 1981; Athanasiadis et al. 2010; Franzke et al. 2011; Winters et al. 2019b). The relationship between atmospheric teleconnections and the NPJ is investigated through considering SOM node frequency changes during Pacific–North American (PNA), Arctic Oscillation (AO), west Pacific Pattern (WP), and ENSO events.

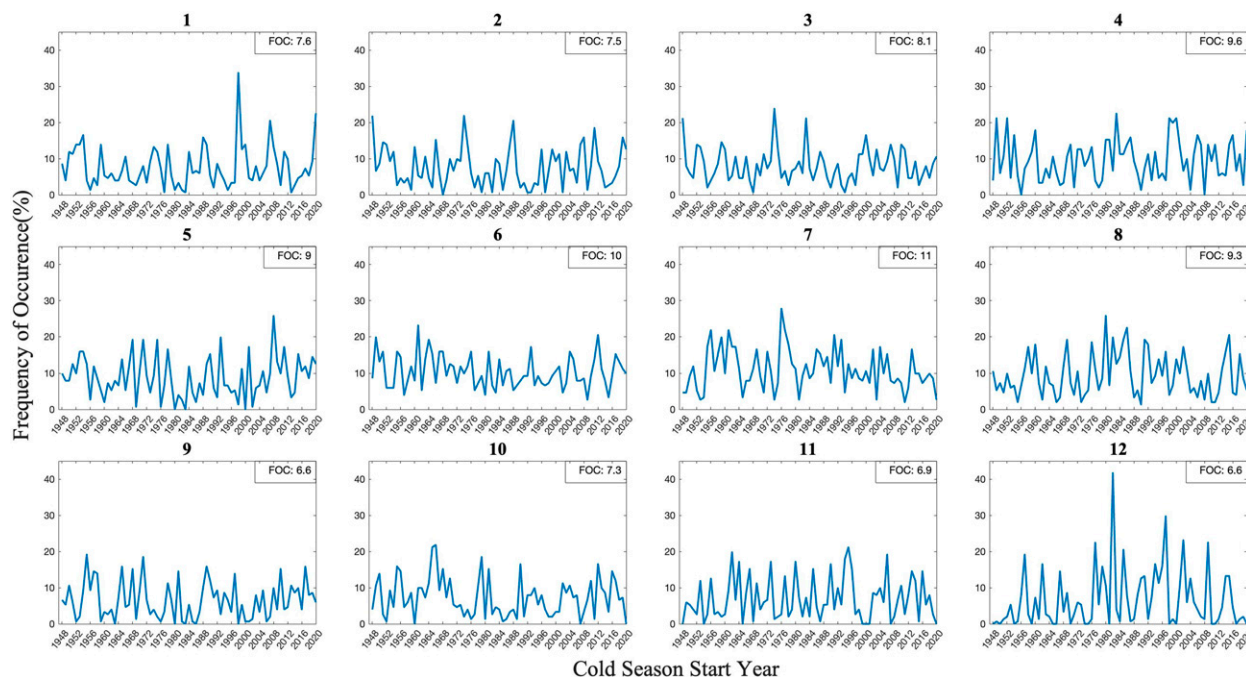


FIG. 8. Percent frequency of occurrence for each SOM node during each cold season.

The PNA is a dominant, wavelike anomaly teleconnection pattern in the NH boreal winter that drives temperature and precipitation anomalies in North America and is associated with fluctuations within the NPJ (e.g., [Dickson and Namias 1976](#); [Barnston and Livezey 1987](#); [Franzke et al. 2011](#); [Griffin and Martin 2017](#); [Henderson et al. 2020](#)). In its positive phase, anomalous troughs sit over the North Pacific and southeastern United States, and anomalous ridges are located over the subtropical North Pacific and the intermountain west of North America. The juxtaposition of the anomalous trough and ridge over the North Pacific supports enhanced westerly flow between them and, subsequently, an enhanced and extended NPJ. The negative phase of the PNA, on the other hand, is characterized by anomalous ridges over the North Pacific and eastern United States and an anomalous trough over the western United States. The anomalous ridge over the North Pacific, often associated with blocking activity, would support enhanced anomalous easterly flow within the vicinity of the NPJ exit region, leading to a jet retraction or equatorward deflection.

Daily PNA index values from the Climate Prediction Center (CPC) are utilized to separate SOM FOC into three categories: positive PNA events with an index above  $1\sigma$ , negative PNA events with an index below  $-1\sigma$ , and a neutral PNA with an index between  $-1\sigma$  and  $1\sigma$ . [Figure 10a](#) illustrates the disparity of SOM node frequency between positive and negative PNA events. As expected, positive PNA events are largely characterized by jet extensions. Node 8 is the dominant pattern characterizing positive PNA events, with an FOC near 30%, followed by nodes 4 at 22% and 12 at 18%. This is in stark contrast to negative PNA events, which are largely characterized by nodes 5, 9, 10, and 11—variations of jet retractions and/or a split jet with equatorward and poleward components. Overall, it is evident that the frequencies of many of

the SOM nodes are well associated with the PNA, with statistically significant differences in FOC from neutral PNA events. The nodes exhibiting the weakest relationship with the PNA are nodes 1 and 2, which are both characterized by a reduced FOC during both positive and negative PNA events.

Another dominant NH teleconnection pattern strongly tied to weather and climate variations is the Arctic Oscillation (AO) ([Thompson and Wallace 1998](#); [Higgins et al. 2000](#)). During a positive AO, anomalously low pressure lies over the Arctic, whereas anomalously high pressure sits over the North Pacific and Atlantic basins. The negative phase is characterized by a similar pattern but of opposite sign. As in the PNA analysis, daily CPC AO indices are employed and partitioned into positive AO events (index  $> 1\sigma$ ), negative AO events ( $< -1\sigma$ ) and neutral AO events (between  $-1\sigma$  and  $1\sigma$ ). [Figure 10b](#) reveals that positive AO events are most frequently characterized by nodes 5 and 9, whereas negative AO events are most frequently characterized by nodes 8, 7, and 12. However, the FOC is more evenly distributed during AO events than for PNA events, with departures from the climatological FOC remaining below 4% for most of the nodes and few statistically significant differences between positive and negative AO events from neutral events. Nodes 8, 5, and 12 illustrate the largest disparity between positive and negative AO events, which suggests that they are more strongly associated with the AO teleconnection pattern.

A third major mode of wintertime low-frequency variability over the North Pacific is the west Pacific (WP) pattern ([Wallace and Gutzler 1981](#); [Barnston and Livezey 1987](#)). Characterized by a lower tropospheric north-south dipole anomaly over the Pacific and upper tropospheric wave train-like anomalies, the WP pattern is associated with variations in the North Pacific jet stream and sensible weather impacts both upstream and downstream.

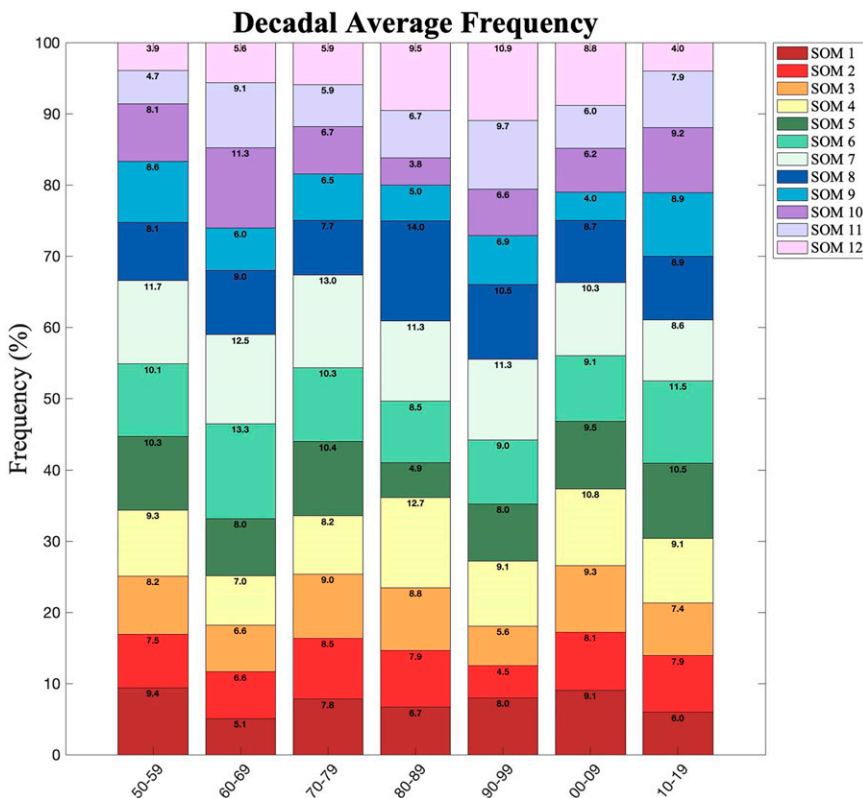


FIG. 9. Decadal mean of frequency of occurrence for each SOM node beginning with 1950.

As in the above analyses, WP indices from the CPC are employed and stratified into positive WP events ( $\text{index} > 1\sigma$ ) negative WP events ( $< 1\sigma$ ) and neutral WP (between  $-1\sigma$  and  $1\sigma$ ). During a positive WP pattern, retractions characterized by nodes 1 and 5 exhibit statistically significant increases in frequency, whereas extensions/equatorward deflections characterized by nodes 11 and 12 exhibit statistically significant decreases in frequency (Fig. 10c). In the negative phase of the WP pattern, node 1 frequency decreases whereas nodes 7, 11, and 12 increase in frequency. Unlike during AO and PNA events, nodes 1 and 11 exhibit considerable fluctuations in FOC depending on the phase of the WP.

As evidenced by the correlation between the time series of node 12 seasonal FOC and the ENSO index (0.54), the SOM node frequency distribution is also associated with ENSO events. This relationship is examined through applying the Niño-3.4 index and distinguishing between El Niño events (Niño-3.4 index  $> 1^\circ\text{C}$ ), La Niña events ( $< -1^\circ\text{C}$ ), and a neutral ENSO (between  $-1^\circ\text{C}$  and  $1^\circ\text{C}$ ). As for the PNA and AO events, FOC is then calculated during each of the three categories. Illustrated in Fig. 10d, it is unsurprising that El Niño events are most frequently accompanied by jet extensions (nodes 8 and 12). Conversely, La Niña events are most frequently associated with retractions and/or poleward deflections (nodes 1, 2, and 3), as well as node 4. However, as in the frequency distribution during AO events, the discrepancies in FOC between positive and negative events are much lower

than the discrepancies evident during PNA events, with node 12 exhibiting the largest FOC difference between events. The more substantial SOM node FOC changes associated with PNA events could be a reflection of the extratropical eddy dynamics largely influencing PNA growth through interactions with the jet stream (e.g., Simmons et al. 1983; Borges and Hartmann 1992; Borges and Sardeshmukh 1995; Mori and Watanabe 2008; Franzke et al. 2011).

*MJO and SOM nodes*

Another important teleconnection that has been tied to changes within the NPJ is the MJO. The MJO is the leading mode of tropical intraseasonal variability and is characterized by anomalous tropical convection migrating east from the Indian Ocean toward the Pacific in 30–60-day cycles (e.g., Madden and Julian 1971). The anomalous convection associated with the MJO, like the anomalous convection associated with ENSO events, can act as a point source for Rossby waves generated by the associated upper-tropospheric horizontal divergence and latent heating (Hoskins and Karoly 1981; Kiladis and Weickmann 1992). The subsequent Rossby wave train can then propagate eastward and poleward into the vicinity of the NPJ, interacting with the extratropical flow. However, the time scale and intensity of the Rossby wave train’s propagation from the tropics into the extratropics are dependent not only on the longitudinally varying extratropical basic state, but also on the initial longitudinal location of the enhanced

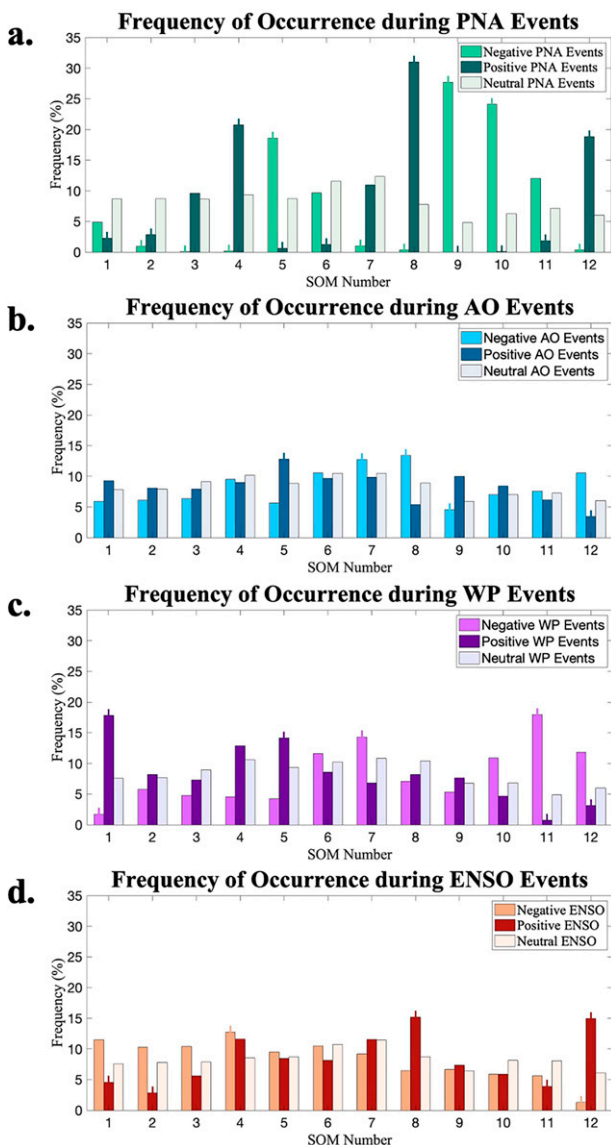


FIG. 10. Frequency of occurrence of each SOM node for days characterized by (a) PNA events, (b) AO events, (c) WP events, and (d) ENSO events. Statistically significant FOC departures from neutral conditions at the 95% confidence interval (determined from a two-tailed test) are denoted with a tick over the bar.

convection (Hoskins and Ambrizzi 1993; Jin and Hoskins 1995). Therefore, the MJO, a longitudinally propagating heat source, is a complicated and important teleconnection to consider for wintertime extratropical variability.

Following a method similar to that employed by Cassou (2008) and Lee et al. (2020), the influence of the MJO on the 12 SOM jet states is investigated through calculating the percent change in anomalous frequency of occurrence of the 12 nodes following strong MJO phases (Figs. 11–13). The percent change is calculated at each lag between 1 and 16 days following the strong MJO phase. Strong MJO events are identified using the real-time multivariate MJO (RMM) indices

from the Australian Bureau of Meteorology for 1979–2020 NDJFM cold seasons (Wheeler and Hendon 2004; <http://www.bom.gov.au/climate/mjo/>). The indices consist of RMM1 and RMM2, defined by the leading two EOF/PCs of satellite-observed outgoing longwave radiation anomalies and 850- and 200-hPa zonal wind anomalies. MJO amplitude is determined by  $\sqrt{\text{RMM1}^2 + \text{RMM2}^2}$ , in which amplitudes greater than  $1\sigma$  are considered. The MJO phases are then organized into nine phases—phases 1–8 are the phases described above and as in Wheeler and Hendon (2004), and phase 0 consists of days in which the amplitude is  $<1$ . Additionally, ENSO events are filtered to remove constructive or destructive interference that might impact the MJO signal on jet node FOC. As in Lee et al. (2020), anomalous occurrences are subjected to two significance tests. The first is a  $\chi^2$  test for the anomalous frequency distribution of the 12 SOM nodes together at each MJO phase and lag, and the second is a binomial test for the individual nodes. Statistical significance is established only if the anomalous FOC passes both the  $\chi^2$  test at the 99% confidence interval and the binomial test at the 95% confidence interval.

In comparing SOM nodes featuring jet retractions, jet extensions, poleward deflections, equatorward deflections, and weaker anomalies, the existence of statistically significant anomalous occurrences and a slope as a function of lag following active MJO phases indicates a MJO forcing. Beginning with MJO events during a neutral ENSO state, the retraction and equatorward deflection denoted by node 9 illustrates the largest increase in anomalous occurrence during MJO phase 1, approaching 200% in the following week (Fig. 11). By MJO phases 2 and 3, however, the retraction denoted by node 5 exhibits enhanced frequencies, while node 9 shifts from a  $>100\%$  increase in the 5 days following phase 2, to an  $\sim 50\%$  decrease by day 10. Although nodes 9, 10, and 11 all feature equatorward deflections, nodes 9 and 5 are characterized by stronger negative anomalies in the climatological jet exit region, suggesting that earlier phases of the MJO are associated more strongly with negative zonal wind anomalies confined to the jet exit region. Extended nodes 8 and 12 also have reduced frequencies between 50% and 100% during the early MJO phases. During the middle phases of the MJO (phases 3–6), nodes 5 and 9 exhibit significant reduced regime frequency in the following 2–14 days, whereas the extension denoted by node 12 begins to increase in FOC in the week following MJO phase 4. Between MJO phases 5 and 7, the anomalous frequencies for node 12 approach 150%. The increase in node 12 FOC is attended by a decrease in FOC of nodes 5 and 9. However, by MJO phase 7, node 9 shifts again from negative anomalous frequencies between 1 and 5 days to positive anomalous frequencies in the 7–14 days following the active phase. Overall, the nodes most strongly tied to the progression of the MJO during ENSO neutral events are nodes 5, 9, and 12.

The anomalous frequency distribution for MJO events during El Niño episodes illustrates key statistical differences. During El Niño episodes, MJO phase 1 is largely characterized by increases in node 9 and 12 FOC (Fig. 12). However, the retracted node 9 only increases in frequency beyond lag 7, whereas extended node 12 begins to slope downward beyond

## Anomalous FOC During MJO and Neutral ENSO

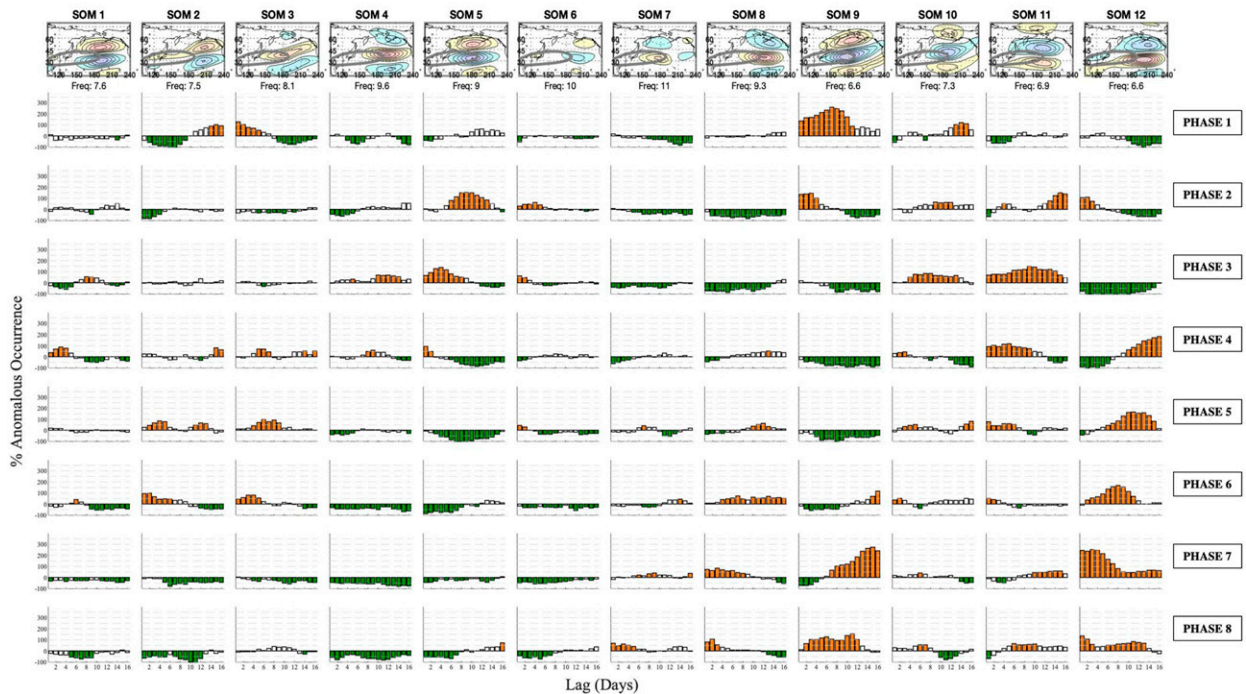


FIG. 11. Lagged relationships between the eight phases of the MJO and SOM nodes during ENSO neutral events. For each active MJO phase, ( $RMM > 1$ ), the anomalous FOC of SOM nodes is plotted as a function of lag from 1 to 16 days after the active MJO phase. A 100% anomalous FOC denotes an FOC twice that of the climatological FOC for the SOM node, whereas a  $-100\%$  anomalous occurrence denotes an FOC of 0. Orange (green) shading denote statistically significant anomalous FOC as determined from a  $\chi^2$  test and binomial test.

lag 5. MJO phases 2 and 3 are not as discriminative for SOM node regimes, with either a weak or nonexistent slope as a function of lag for most of the nodes. By MJO phase 4, with enhanced convection migrating into the west Pacific, nodes 5 and 9 begin to decrease in anomalous occurrence, while node 12 exhibits a gradual increase over lags 7–16. Between MJO phases 5 and 8, the anomalous FOC for node 12 reaches 200%–300%, exhibiting much larger anomalous occurrences than during neutral ENSO MJO phases 5–8. The extension characterized by node 8 also experiences an increase in FOC between 100% and 150%, whereas nodes 1, 2, 3, 5, and 9 reduce in FOC within the later phases of the MJO.

The anomalous FOC during active MJO phases and La Niña episodes (Fig. 13) illustrate even stronger statistical differences when compared to ENSO neutral and El Niño episodes. For example, MJO phase 1 is no longer largely characterized by SOM node 9 or 12, but rather by substantial frequency increases in node 1 at lags 4–16. This is in stark contrast to El Niño and ENSO neutral events, in which the MJO has little to no influence on node 1. The influence of the MJO on node 1 FOC is evident from phases 1 to 6. Also during the early MJO phases, nodes 7, 8, 10, 11, and 12 all exhibit a reduction in frequency. Middle MJO phases 3 through 5, however, appear to have an impact on equatorward deflected node 2, with anomalous frequencies exceeding 150%, while extended node 12 depicts a

strong frequency reduction between phases 3 and 5. Between MJO phases 6 and 8, there are no substantial increases in FOC for any of the nodes; however, retracted and/or equatorward deflected nodes 9 and 10 exhibit reduced frequencies.

Overall, the lagged relationships between the MJO phases and anomalous SOM node occurrences illustrated in Figs. 11–13 demonstrate teleconnections patterns consistent with previous findings and provide a more detailed and nuanced analysis of the subtleties of the jet stream anomalies corresponding to specific MJO phases. Separation of strong MJO events between ENSO neutral, ENSO positive, and ENSO negative also illustrates the importance of stratifying ENSO phase when investigating MJO teleconnections. In particular, retracted and/or equatorward deflected nodes 5 and 9 contribute the most to the increased frequencies associated with MJO phases 1–2 during ENSO neutral events, with enhanced convection over the Indian Ocean and suppressed convection in the Pacific basin. MJO phase 4, on the other hand, is not as discriminative for the jet regime. The later phases of the MJO are largely characterized by increases in extended node 12 FOC, when the enhanced convection migrates over the Pacific basin. The large increases in node 12 FOC during MJO phases 1 and 4–8 during El Niño events can be attributed largely to ENSO, given that the FOC during ENSO positive events (Fig. 10d) was over double the climatological FOC. However, there is a slope as a function of

## Anomalous FOC During MJO and Positive ENSO

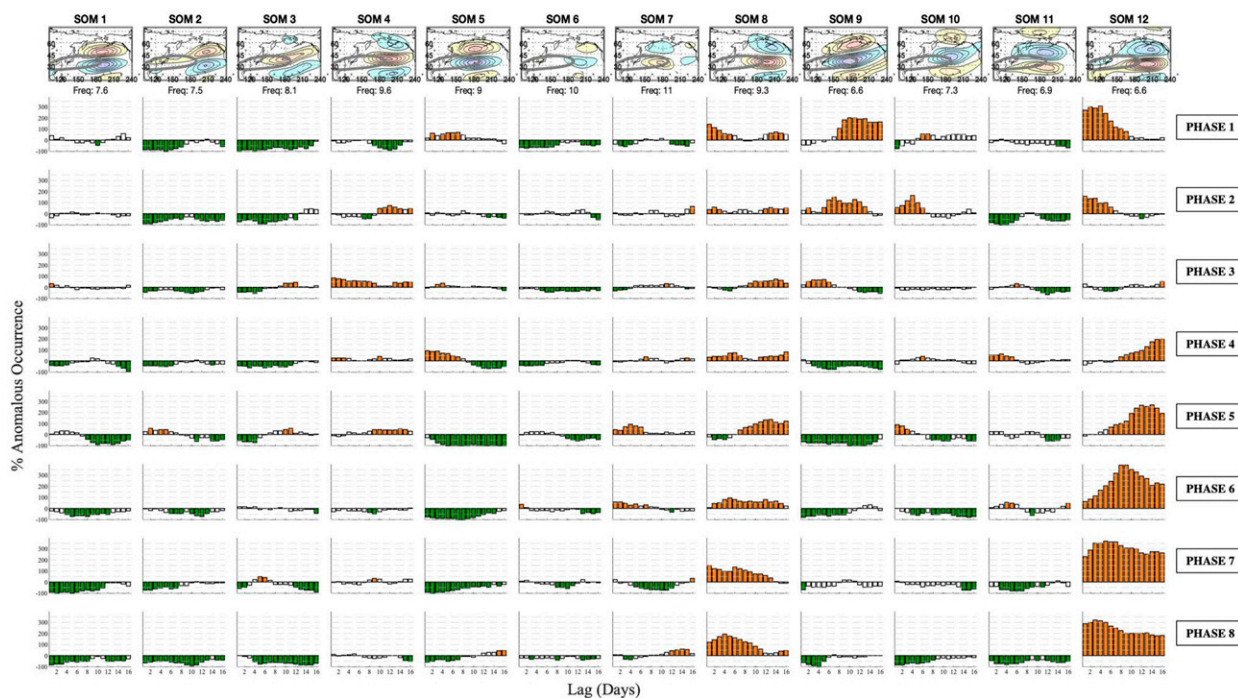


FIG. 12. As in Fig. 11, but during positive ENSO events.

lag evident in both ENSO neutral and ENSO positive episodes for node 12, suggesting that the MJO is a precursor to node 12 jet extensions. This relationship is not as robust for other extensions denoted by node 8 and 4, which further establishes the importance of complementing the previous EOF-identified four-pattern model of NPJ variability with the greater detail afforded by the SOM analysis. The teleconnections for the MJO during La Niña episodes are much different. Unsurprisingly, extended nodes 8 and 12 exhibit negative or insignificant anomalous frequencies, as convection over the tropical east Pacific is suppressed. SOM nodes 1 and 2, however, were characterized by the largest increases in FOC following early and middle phases of the MJO. While these large increases were only noted during La Niña episodes, the minimal increases in FOC during La Niña illustrated in Fig. 10 suggests that constructive interference between early phases of the MJO and La Niña leads to large increases in nodes 1 and 2 FOC.

## 5. Conclusions

A novel self-organizing maps analysis is applied to 250-hPa zonal winds over 73 NDJFM cold seasons to better understand variability within the wintertime NPJ. Prior work in understanding intraseasonal NPJ variability has proceeded from identification of the leading modes of variability: a zonal extension or retraction and a meridional deflection of the jet exit region, as depicted in EOF/PC analysis (e.g., Athanasiadis et al. 2010; Jaffe et al. 2011; Griffin and Martin 2017; Breeden and Martin 2018; Winters et al. 2019a,b). The SOM analysis described here

expands and complements previous EOF/PC analysis, identifying 12 archetypal NPJ patterns resembling variations of the extended/retracted and poleward/equatorward deflected patterns of EOF-based NPJ variability (e.g., Schubert and Park 1991; Athanasiadis et al. 2010; Jaffe et al. 2011), as well as new complex modes of variability not captured by these previous analyses. Examples of these include an enhancement of the jet characterized by node 7, a poleward deflected jet jutting into the Gulf of Alaska characterized by node 2, and a split jet with extratropical and subtropical counterparts denoted by nodes 9 and 10.

The expanded SOM-based jet regimes add important detail characterizing wintertime NPJ variability. For example, composites of Z500, SLP, and 850T illustrate that seemingly minor variations in EOF1- and EOF2-like patterns are tied to distinct differences in synoptic-scale anomalies over the Pacific and North America and both upstream and downstream low-level temperature anomalies. Additionally, investigation of intraseasonal, interannual, and decadal variability of SOM node FOC reveals that there is variability at both the inter- and intraseasonal time scales. Seasonally, November is characterized by a higher FOC of poleward and/or extended jet nodes 3 and 4, as well as of a retracted and equatorward deflected node 10. Conversely, extended node 12 has its lowest FOC in November (2.2%). Mild variations are noted between December, January, and February, with jet extensions becoming more frequent and peaking in January and February. By March, retracted nodes 1 and 5 become more common.

The FOC for each node varies even more substantially at interannual time scales, with no statistically significant trend.

## Anomalous FOC During MJO and Negative ENSO

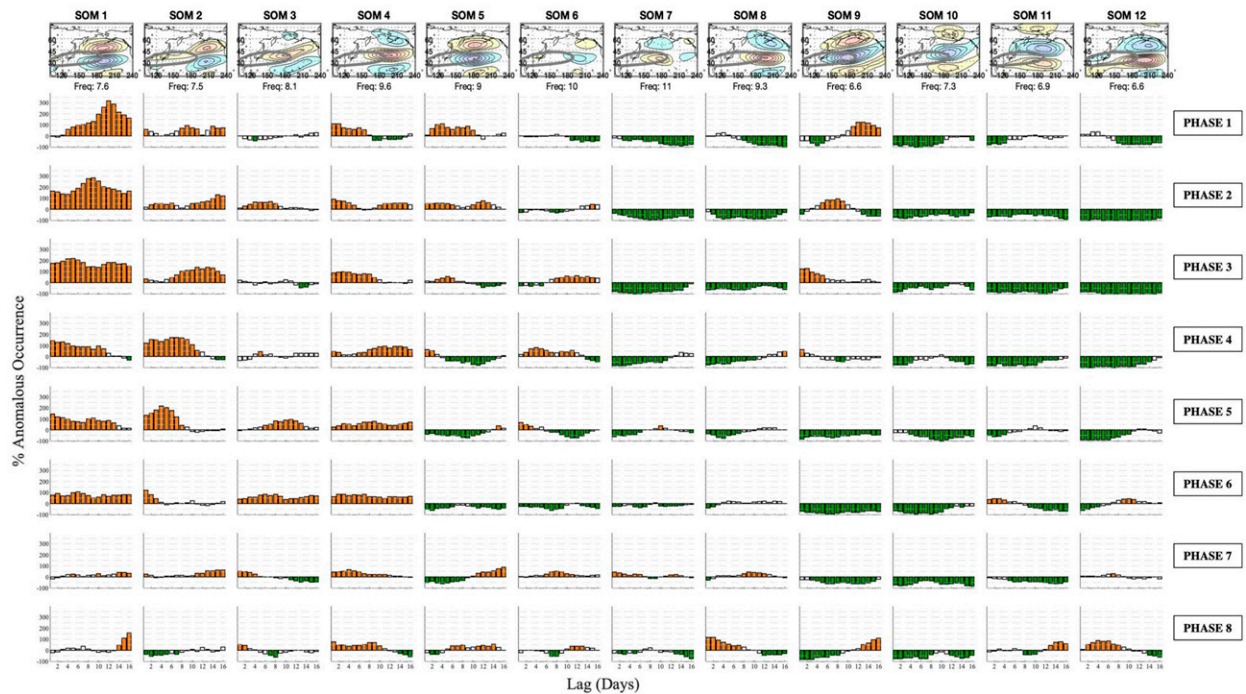


FIG. 13. As in Fig. 11, but during negative ENSO events.

Nevertheless, the interannual variation is evidenced to be, in part, tied to teleconnection patterns like the PNA, AO, WP, ENSO, and MJO. Node 12 exhibited one of the strongest relationships to the PNA, AO, and ENSO and the longest mean residence time. These characteristics further distinguish a node 12 jet extension from an extension  $5^{\circ}$ – $10^{\circ}$  farther north (nodes 4 and 8). Conversely, node 1 exhibited one of the weakest relationships to the aforementioned teleconnection patterns, but one of the strongest to the WP. Moreover, in examining anomalous FOC associated with strong MJO events during La Niña episodes, the signal for node 1 suggested an MJO influence, more than doubling its FOC following early phases of the MJO. During ENSO neutral or El Niño episodes, however, early phases of the MJO coincided with, or preceded FOC increases in node 9. These teleconnection patterns provide insight into the varying nature of SOM nodes at inter- and intra-seasonal time scales, and suggest that seemingly similar NPJ patterns like nodes 5 and 9 or nodes 4, 8, and 12 can be driven by different extratropical and/or tropical processes. Utilizing the SOM nodes to characterize NPJ variability is, therefore, likely to prove valuable in better understanding how tropical and extratropical processes interact with the jet stream.

Additionally, use of the SOM nodes has the potential to inform medium range forecasting skill. In comparing the best to the worst GEFS forecasts initialized during EOF/PC-identified NPJ regimes, Winters et al. (2019b) revealed that there were key differences in the synoptic scale structure within each regime. For example, for forecasts initialized during an extended regime, the worst forecasts emerged from a synoptic-scale

environment characterized by higher geopotential height anomalies over the eastern North Pacific and North America (Winters et al. 2019b, their Fig. 12b), which resembles the synoptic scale environment of SOM node 8 and a positive PNA-like structure (Fig. 4h), whereas the best forecasts emerged from an environment more characteristic of SOM node 12 (Winters et al. 2019b, their Fig. 12a). This suggests that subtle  $5^{\circ}$ – $10^{\circ}$  latitudinal displacements of the NPJ extension are likely tied not only to specific teleconnections like the PNA and MJO but also to downstream, medium-range forecast skill. Accordingly, we suggest that a better understanding of NPJ transitions, including the likelihood and nature of transitions between common wintertime NPJ patterns, may make a fundamental contribution to improving predictability at these time scales. Therefore, subsequent work builds upon the results presented here to characterize jet variability through consideration of transitions among the 12 SOM nodes at short (5 day), midrange (10 day), and longer-range (15 and 20 day) time scales.

*Acknowledgments.* Support for this work is provided by the National Science Foundation under Grant NSF-16400455 and NSF-2055667 as well as from Ned P. Smith Professorship of Climatology (granted to the second author) by the University of Wisconsin–Madison. The authors thank Professors Daniel Vimont, Stephanie Henderson, and Michael Morgan at the University of Wisconsin–Madison for their insightful discussions and constructive feedback. Additionally, Dr. Melissa Gervais and an anonymous reviewer have provided valuable suggestions and comments for the presentation of this work.

*Data availability statement.* NCEP Reanalysis data are provided by the NOAA/OAR/ESRL PSL, Boulder, Colorado, and available at <https://psl.noaa.gov/data/gridded/data.ncep.reanalysis.html>. Real-time multivariate Madden–Julian oscillation indices are provided from the Australian Bureau of Meteorology and available at <http://www.bom.gov.au/climate/mjo/>. Teleconnection data and indices (PNA, AO, ENSO) are provided by the Climate Prediction Center and available at [https://www.cpc.ncep.noaa.gov/products/precip/CWlink/daily\\_ao\\_index/teleconnections.shtml](https://www.cpc.ncep.noaa.gov/products/precip/CWlink/daily_ao_index/teleconnections.shtml).

## REFERENCES

- Athanasiadis, P. J., J. M. Wallace, and J. J. Wettstein, 2010: Patterns of wintertime jet stream variability and their relation to the storm tracks. *J. Atmos. Sci.*, **67**, 1361–1381, <https://doi.org/10.1175/2009JAS3270.1>.
- Barnston, A. G., and R. E. Livezey, 1987: Classification, seasonality, and persistence of low frequency atmospheric circulation patterns. *Mon. Wea. Rev.*, **115**, 1083–1126, [https://doi.org/10.1175/1520-0493\(1987\)115<1083:CSAPOL>2.0.CO;2](https://doi.org/10.1175/1520-0493(1987)115<1083:CSAPOL>2.0.CO;2).
- Borges, M. D., and D. L. Hartmann, 1992: Barotropic instability and optimal perturbations of observed nonzonal flows. *J. Atmos. Sci.*, **49**, 335–354, [https://doi.org/10.1175/1520-0469\(1992\)049<0335:BIAOPO>2.0.CO;2](https://doi.org/10.1175/1520-0469(1992)049<0335:BIAOPO>2.0.CO;2).
- , and P. D. Sardeshmukh, 1995: Barotropic Rossby wave dynamics of zonally varying upper-level flows during northern winter. *J. Atmos. Sci.*, **52**, 3779–3796, [https://doi.org/10.1175/1520-0469\(1995\)052<3779:BRWDOZ>2.0.CO;2](https://doi.org/10.1175/1520-0469(1995)052<3779:BRWDOZ>2.0.CO;2).
- Breedeen, M., and J. E. Martin, 2018: Analysis of the initiation of an extreme North Pacific jet retraction using piecewise tendency diagnosis. *Quart. J. Roy. Meteor. Soc.*, **144**, 1895–1913, <https://doi.org/10.1002/qj.3388>.
- , and —, 2019: Evidence for nonlinear processes in fostering a North Pacific jet retraction. *Quart. J. Roy. Meteor. Soc.*, **145**, 1559–1570, <https://doi.org/10.1002/qj.3512>.
- Cassano, E. N., A. H. Lynch, J. J. Cassano, and M. R. Koslow, 2006: Classification of synoptic patterns in the western Arctic associated with extreme events at Barrow, Alaska, USA. *Climate Res.*, **30**, 83–97, <https://doi.org/10.3354/cr030083>.
- Cassou, C., 2008: Intraseasonal interaction between the Madden–Julian oscillation and the North Atlantic oscillation. *Nature*, **455**, 523–527, <https://doi.org/10.1038/nature07286>.
- Chu, P.-S., A. J. Nash, and F.-Y. Porter, 1993: Diagnostic studies of two contrasting rainfall episodes in Hawaii: Dry 1981 and wet 1982. *J. Climate*, **6**, 1457–1462, [https://doi.org/10.1175/1520-0442\(1993\)006<1457:DSOTCR>2.0.CO;2](https://doi.org/10.1175/1520-0442(1993)006<1457:DSOTCR>2.0.CO;2).
- Cohen, S. J., 1983: Classification of 500 mb height anomalies using obliquely rotated principal components. *J. Appl. Meteor. Climatol.*, **22**, 1975–1988, [https://doi.org/10.1175/1520-0450\(1983\)022<1975:COMHAU>2.0.CO;2](https://doi.org/10.1175/1520-0450(1983)022<1975:COMHAU>2.0.CO;2).
- Cook, A. R., L. M. Leslie, D. B. Parsons, and J. T. Schaefer, 2017: The impact of the El Niño–Southern Oscillation (ENSO) on winter and early spring U.S. tornado outbreaks. *J. Appl. Meteor. Climatol.*, **56**, 2455–2478, <https://doi.org/10.1175/JAMC-D-16-0249.1>.
- Delcambre, S. C., D. J. Lorenz, D. J. Vimont, and J. E. Martin, 2013: Diagnosing Northern Hemisphere jet portrayal in 17 CMIP3 global climate models: Twentieth-century intermodal variability. *J. Climate*, **26**, 4910–4929, <https://doi.org/10.1175/JCLI-D-12-00337.1>.
- Dickson, R. R., and J. Namias, 1976: North American influences on the circulation and climate of the North Atlantic sector. *Mon. Wea. Rev.*, **104**, 1255–1265, [https://doi.org/10.1175/1520-0493\(1976\)104<1255:NAIOTC>2.0.CO;2](https://doi.org/10.1175/1520-0493(1976)104<1255:NAIOTC>2.0.CO;2).
- Franzke, C., T. Woollings, and O. Martius, 2011: Persistent circulation regimes and preferred regime transitions in the North Atlantic. *J. Atmos. Sci.*, **68**, 2809–2825, <https://doi.org/10.1175/JAS-D-11-046.1>.
- Gervais, M., E. Atallah, J. R. Gyakum, and L. Bruno Tremblay, 2016: Arctic air masses in a warming world. *J. Climate*, **29**, 2359–2373, <https://doi.org/10.1175/JCLI-D-15-0499.1>.
- Griffin, K. S., and J. E. Martin, 2017: Synoptic features associated with temporally coherent modes of variability of the North Pacific jet stream. *J. Climate*, **30**, 39–54, <https://doi.org/10.1175/JCLI-D-15-0833.1>.
- Gu, Q., and M. Gervais, 2021: Exploring North Atlantic and North Pacific decadal climate prediction using self-organizing maps. *J. Climate*, **34**, 123–141, <https://doi.org/10.1175/JCLI-D-20-0017.1>.
- Hannachi, A., 2004: *A Primer for EOF Analysis of Climate Data*. University of Reading, 33 pp.
- Henderson, S. A., D. J. Vimont, and M. Newman, 2020: The critical role of non-normality in partitioning tropical and extratropical contributions to PNA growth. *J. Climate*, **33**, 6273–6295, <https://doi.org/10.1175/JCLI-D-19-0555.1>.
- Hewitson, B. C., and R. G. Crane, 2002: Self-organizing maps: Applications to synoptic climatology. *Climate Res.*, **22**, 13–26, <https://doi.org/10.3354/cr022013>.
- Higgins, R. W., A. Leetmaa, Y. Xue, and A. Barnston, 2000: Dominant factors influencing the seasonal predictability of U.S. precipitation and surface air temperature. *J. Climate*, **13**, 3994–4017, [https://doi.org/10.1175/1520-0442\(2000\)013<3994:DFITSP>2.0.CO;2](https://doi.org/10.1175/1520-0442(2000)013<3994:DFITSP>2.0.CO;2).
- Hope, P. K., W. Drosowsky, and N. Nicholls, 2006: Shifts in synoptic systems influencing southwest Western Australia. *Climate Dyn.*, **26**, 751–764, <https://doi.org/10.1007/s00382-006-0115-y>.
- Horel, J. D., and J. M. Wallace, 1981: Planetary-scale atmospheric phenomena associated with the Southern Oscillation. *Mon. Wea. Rev.*, **109**, 813–829, [https://doi.org/10.1175/1520-0493\(1981\)109<0813:PSAPAW>2.0.CO;2](https://doi.org/10.1175/1520-0493(1981)109<0813:PSAPAW>2.0.CO;2).
- Hoskins, B. J., and D. J. Karoly, 1981: The steady linear response of a spherical atmosphere to thermal and orographic forcing. *J. Atmos. Sci.*, **38**, 1179–1196, [https://doi.org/10.1175/1520-0469\(1981\)038<1179:TSLROA>2.0.CO;2](https://doi.org/10.1175/1520-0469(1981)038<1179:TSLROA>2.0.CO;2).
- , and T. Ambrizzi, 1993: Rossby wave propagation on a realistic longitudinally varying flow. *J. Atmos. Sci.*, **50**, 1661–1671, [https://doi.org/10.1175/1520-0469\(1993\)050<1661:RWPOAR>2.0.CO;2](https://doi.org/10.1175/1520-0469(1993)050<1661:RWPOAR>2.0.CO;2).
- Jaffe, S. C., J. E. Martin, D. J. Vimont, and D. J. Lorenz, 2011: A synoptic climatology of episodic, subseasonal retractions of the Pacific jet. *J. Climate*, **24**, 2846–2860, <https://doi.org/10.1175/2010JCLI3995.1>.
- Jin, F., and B. J. Hoskins, 1995: The direct response to tropical heating in a baroclinic atmosphere. *J. Atmos. Sci.*, **52**, 307–319, [https://doi.org/10.1175/1520-0469\(1995\)052<0307:TDRITH>2.0.CO;2](https://doi.org/10.1175/1520-0469(1995)052<0307:TDRITH>2.0.CO;2).
- Johnson, N. C., and S. B. Feldstein, 2010: The continuum of North Pacific sea level pressure patterns: Intraseasonal, interannual, and interdecadal variability. *J. Climate*, **23**, 851–867, <https://doi.org/10.1175/2009JCLI3099.1>.
- Kalnay, E., and Coauthors, 1996: The NCEP/NCAR 40-Year Reanalysis Project. *Bull. Amer. Meteor. Soc.*, **77**, 437–472, [https://doi.org/10.1175/1520-0477\(1996\)077<0437:TNYRP>2.0.CO;2](https://doi.org/10.1175/1520-0477(1996)077<0437:TNYRP>2.0.CO;2).
- Kiladis, G. N., and K. M. Weickmann, 1992: Circulation anomalies associated with tropical convection during northern winter.

- Mon. Wea. Rev.*, **120**, 1900–1923, [https://doi.org/10.1175/1520-0493\(1992\)120<1900:CAAATC>2.0.CO;2](https://doi.org/10.1175/1520-0493(1992)120<1900:CAAATC>2.0.CO;2).
- Kohonen, T., 1982: Self-organized formation of topologically correct feature maps. *Biol. Cybern.*, **43**, 59–69, <https://doi.org/10.1007/BF00337288>.
- , 1998: The self-organizing map. *Neurocomputing*, **21**, 1–6, [https://dx.doi.org/10.1016/S0925-2312\(98\)00030-7](https://dx.doi.org/10.1016/S0925-2312(98)00030-7).
- , 2001: *Self-Organizing Maps*. 3rd ed. Springer-Verlag, 502 pp.
- Kutzbach, J. E., 1967: Empirical eigenvectors of sea-level pressure, surface temperature and precipitation complexes over North America. *J. Appl. Meteor.*, **6**, 791–802, [https://doi.org/10.1175/1520-0450\(1967\)006<0791:EEOSLP>2.0.CO;2](https://doi.org/10.1175/1520-0450(1967)006<0791:EEOSLP>2.0.CO;2).
- Lee, J. C. K., R. W. Lee, S. J. Woolnough, and L. J. Boxall, 2020: The links between the Madden-Julian oscillation and European weather regimes. *Theor. Appl. Climatol.*, **141**, 567–586, <https://doi.org/10.1007/s00704-020-03223-2>.
- Li, C., and J. J. Wettstein, 2012: Thermally driven and eddy-driven jet variability in reanalysis. *J. Climate*, **25**, 1587–1596, <https://doi.org/10.1175/JCLI-D-11-00145.1>.
- Liu, Y., R. H. Weisberg, and C. N. K. Mooers, 2006: Performance evaluation of the self-organizing map for feature extraction. *J. Geophys. Res.*, **111**, C05018, <https://doi.org/10.1029/2005JC003117>.
- Lorenz, E. N., 1956: Empirical orthogonal functions and statistical weather prediction. Statistical Forecasting Project Scientific Rep. 1, Department of Meteorology, Massachusetts Institute of Technology, Cambridge, MA, 49 pp.
- Lynch, A., P. Uotila, and J. J. Cassano, 2006: Changes in synoptic weather patterns in the polar regions in the 20th and 21st centuries, Part 2: Antarctic. *Int. J. Climatol.*, **26**, 1181–1199, <https://doi.org/10.1002/joc.1305>.
- Madden, R. A., and P. R. Julian, 1971: Detection of a 40–50 day oscillation in the zonal wind in the tropical Pacific. *J. Atmos. Sci.*, **28**, 702–708, [https://doi.org/10.1175/1520-0469\(1971\)028<0702:DOADOI>2.0.CO;2](https://doi.org/10.1175/1520-0469(1971)028<0702:DOADOI>2.0.CO;2).
- Mori, M., and M. Watanabe, 2008: The growth and triggering mechanisms of the PNA: A MJO-PNA coherence. *J. Meteor. Soc. Japan*, **86**, 213–236, <https://doi.org/10.2151/jmsj.86.213>.
- Newman, M., and P. D. Sardeshmukh, 1998: The impact of the annual cycle on the North Pacific/North American response to remote low-frequency forcing. *J. Atmos. Sci.*, **55**, 1336–1353, [https://doi.org/10.1175/1520-0469\(1998\)055<1336:TITOTAC>2.0.CO;2](https://doi.org/10.1175/1520-0469(1998)055<1336:TITOTAC>2.0.CO;2).
- North, G. R., T. L. Bell, R. F. Cahalan, and F. J. Moeng, 1982: Sampling errors in the estimation of empirical orthogonal functions. *Mon. Wea. Rev.*, **110**, 699–706, [https://doi.org/10.1175/1520-0493\(1982\)110<0699:SEITEO>2.0.CO;2](https://doi.org/10.1175/1520-0493(1982)110<0699:SEITEO>2.0.CO;2).
- Otkin, J. A., and J. E. Martin, 2004: The large-scale modulation of subtropical cyclogenesis in the central and eastern Pacific Ocean. *Mon. Wea. Rev.*, **132**, 1813–1828, [https://doi.org/10.1175/1520-0493\(2004\)132<1813:TLMOSC>2.0.CO;2](https://doi.org/10.1175/1520-0493(2004)132<1813:TLMOSC>2.0.CO;2).
- Reusch, D. B., R. B. Alley, and B. C. Hewitson, 2007: North Atlantic climate variability from a self-organizing map perspective. *J. Geophys. Res.*, **112**, D02104, <https://doi.org/10.1029/2006JD007460>.
- Sammon, J. W., 1969: A nonlinear mapping for data structure analysis. *IEEE Trans. Comput.*, **C-18**, 401–409, <https://doi.org/10.1109/T-C.1969.222678>.
- Schubert, S. D., and C.-K. Park, 1991: Low-frequency intraseasonal tropical–extratropical interactions. *J. Atmos. Sci.*, **48**, 629–650, [https://doi.org/10.1175/1520-0469\(1991\)048<0629:LFITEI>2.0.CO;2](https://doi.org/10.1175/1520-0469(1991)048<0629:LFITEI>2.0.CO;2).
- Schuenemann, K. C., and J. J. Cassano, 2009: Changes in synoptic weather patterns and Greenland precipitation in the 20th and 21st centuries: 1. Evaluation of late 20th century simulations from IPCC models. *J. Geophys. Res.*, **114**, D20113, <https://doi.org/10.1029/2009JD011705>.
- , and —, 2010: Changes in synoptic weather patterns and Greenland precipitation in the 20th and 21st centuries: 2. Analysis of 21st century atmospheric changes using self-organizing maps. *J. Geophys. Res.*, **115**, D05108, <https://doi.org/10.1029/2009JD011706>.
- , —, and J. Finnis, 2009: Forcing of precipitation over Greenland: Synoptic climatology for 1961–99. *J. Hydrometeorol.*, **10**, 60–78, <https://doi.org/10.1175/2008JHM1014.1>.
- Simmons, A. J., J. M. Wallace, and G. W. Branstator, 1983: Barotropic wave propagation and instability, and atmospheric teleconnection patterns. *J. Atmos. Sci.*, **40**, 1363–1392, [https://doi.org/10.1175/1520-0469\(1983\)040<1363:BWPAIA>2.0.CO;2](https://doi.org/10.1175/1520-0469(1983)040<1363:BWPAIA>2.0.CO;2).
- Skific, N., J. A. Francis, and J. J. Cassano, 2009a: Attribution of projected changes in atmospheric moisture transport in the Arctic: A self-organizing map perspective. *J. Climate*, **22**, 4135–4153, <https://doi.org/10.1175/2009JCL2645.1>.
- , —, and —, 2009b: Attribution of seasonal and regional changes in Arctic moisture convergence. *J. Climate*, **22**, 5115–5134, <https://doi.org/10.1175/2009JCLI2829.1>.
- Smith, T. M., R. W. Reynolds, R. E. Livezey, and D. C. Stokes, 1996: Reconstruction of sea surface temperature using empirical orthogonal functions. *J. Climate*, **9**, 1403–1420, [https://doi.org/10.1175/1520-0442\(1996\)009<1403:ROHSST>2.0.CO;2](https://doi.org/10.1175/1520-0442(1996)009<1403:ROHSST>2.0.CO;2).
- Thompson, D. W. J., and J. M. Wallace, 1998: The Arctic oscillation signature in the wintertime geopotential height and temperature fields. *Geophys. Res. Lett.*, **25**, 1297–1300, <https://doi.org/10.1029/98GL00950>.
- Vesanto, J., J. Himberg, E. Alhoniemi, and J. Parhankangas, 2000: SOM toolbox for Matlab 5. Helsinki University of Technology Tech. Rep. A57, 60 pp.
- Wallace, J. M., and D. S. Gutzler, 1981: Teleconnections in the geopotential height field during the Northern Hemisphere winter. *Mon. Wea. Rev.*, **109**, 784–812, [https://doi.org/10.1175/1520-0493\(1981\)109<0784:TITGHF>2.0.CO;2](https://doi.org/10.1175/1520-0493(1981)109<0784:TITGHF>2.0.CO;2).
- Wheeler, M. C., and H. H. Hendon, 2004: An all-season real-time multivariate MJO index: Development of an index for monitoring and prediction. *Mon. Wea. Rev.*, **132**, 1917–1932, [https://doi.org/10.1175/1520-0493\(2004\)132<1917:AARMMI>2.0.CO;2](https://doi.org/10.1175/1520-0493(2004)132<1917:AARMMI>2.0.CO;2).
- Wilks, D. S., 2011: *Statistical Methods in the Atmospheric Sciences*. 3rd ed. International Geophysics Series, Vol. 100, Academic Press, 704 pp.
- Winters, A. C., L. F. Bosart, and D. Keyser, 2019a: Antecedent North Pacific jet regimes conducive to the development of continental U.S. extreme temperature events during the cool season. *Wea. Forecasting*, **34**, 393–414, <https://doi.org/10.1175/WAF-D-18-0168.1>.
- , D. Keyser, and L. F. Bosart, 2019b: The development of the North Pacific jet phase diagram as an objective tool to monitor the state and forecast skill of the upper-tropospheric flow pattern. *Wea. Forecasting*, **34**, 199–219, <https://doi.org/10.1175/WAF-D-18-0106.1>.
- Yang, S., K.-M. Lau, and K.-M. Kim, 2002: Variations of the East Asian jet stream and Asian–Pacific–American winter climate anomalies. *J. Climate*, **15**, 306–325, [https://doi.org/10.1175/1520-0442\(2002\)015<0306:VOTEAJ>2.0.CO;2](https://doi.org/10.1175/1520-0442(2002)015<0306:VOTEAJ>2.0.CO;2).